The Model-Data Integration Framework for NASA's Arctic Boreal Vulnerability Experiment (ABoVE)

Author: Eric Stofferahn (329G-Caltech)
Co-Authors: Joshua Fisher (329G), Daniel Hayes (U. Maine), Deborah Huntzinger (Northern Arizona), Christopher Schwalm (Woods Hole)

National Aeronautics and Space Administration

The Benchmarking System

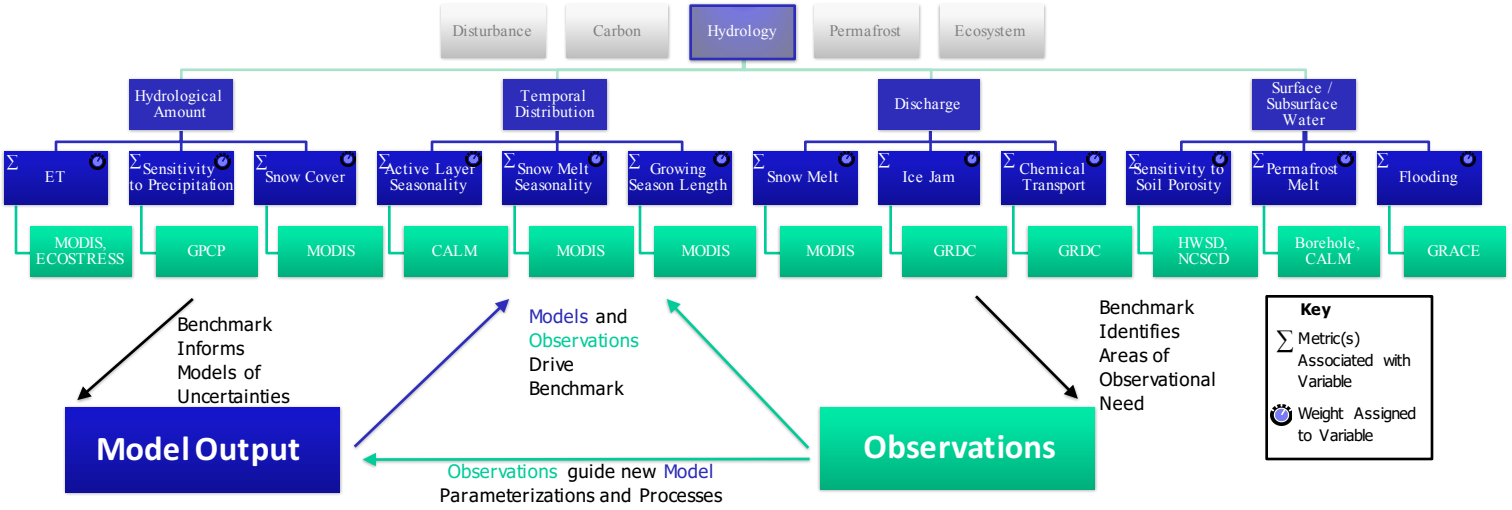

Introduction

The Arctic-Boreal Region (ABR) is a major source of uncertainties for terrestrial biosphere model (TBM) simulations. These uncertainties are precipitated by a lack of observational data from the region, affecting the parameterizations of cold environment processes in the models. Addressing these uncertainties requires a coordinated effort of data collection and integration of the following **5 key indicators** of the ABR ecosystem:

Disturbance

Hydrology

Permafrost

Carbon Pools and Biogeochemistry

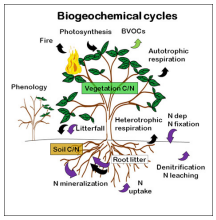

Flora / Fauna and Ecosystem Function

Methods

A model-data integration framework is under development for NASA's **Arctic Boreal Vulnerability Experiment (ABoVE)**, wherein data for the 5 key ABR indicators are used as reference datasets for a benchmarking system which evaluates TBM performance with respect to ABR processes.

North American Carbon Program
MsTMIP
MULTI-SCALE SYNTHESIS AND TERRESTRIAL MODEL INTERCOMPARISON PROJECT

PERMAFROST CARBON NETWORK

CALM
Circumpolar Active Layer Monitoring

Examples of model output sources and dataset observation sources

Website

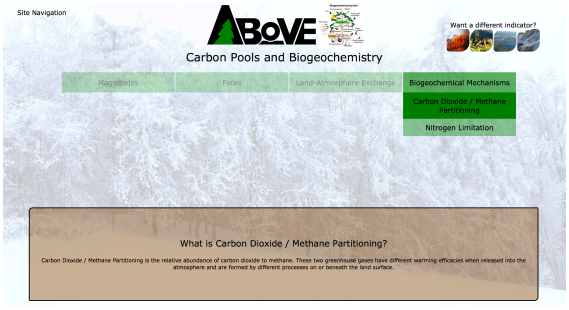

Example of website interface to benchmarking system

Caltech
THE UNIVERSITY OF MAINE
NORTHERN ARIZONA UNIVERSITY
WOODS HOLE RESEARCH CENTER

National Aeronautics and Space Administration
Jet Propulsion Laboratory
California Institute of Technology
Pasadena, California

www.nasa.gov

Poster No.
EA-1

National Aeronautics and Space Administration

Lidar detection of individual trees in tropical forests

António Ferraz (329G) Antonio.A.Ferraz@jpl.nasa.gov
Sassan Saatchi (329G), Clément Mallet, Victoria Meyer (329G)

Motivation

- We intend to characterize the 3D structure of tropical forest at the individual tree crown (ITC) level over large areas using high-resolution lidar across spatial and temporal scales.
- So far, fine scale tropical forest characterization is limited to field sampling techniques over limited study sites. Moreover, field samplings focus on trunk diameter with limitations regarding the measurement of tree height and crown size due to complex and dense vegetation structure.
- The lack of field samplings over space and time is a limitation for the success of satellite missions (e.g. GEDI, NISAR and BIOMASS) regarding their accuracy in mapping the spatial variability of biomass stored in tropical forests.
- Our approach, called Adaptive Mean Shift algorithm (AMS3D), decomposes high-resolution lidar point clouds into 3D clusters corresponding to ITC and enables the direct retrivial many biophysical variables such as tree density and crown size.
- Characterization at the ITC level allows the use of lidar to develop allometric models and analyze forest demography and forest change for simulating forest CO_2 dynamics.
- We tested the AMS3D over two tropical forests: Barro Colorado Island (BCI, Panama) and Mai Ndombe (Republic Democratic of Congo, DRC).

1. AMS3D

1.1. Mean shift

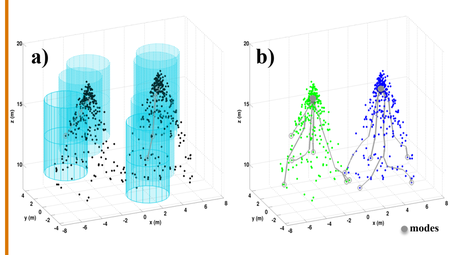

1.2. Single bandwidth

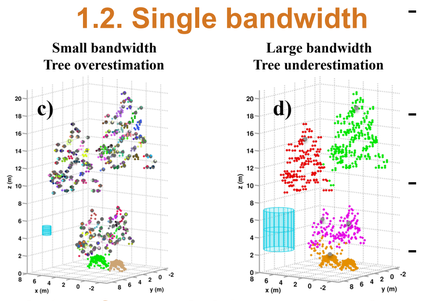

1.3. Adaptive bandwidth accommodates for variable crown size

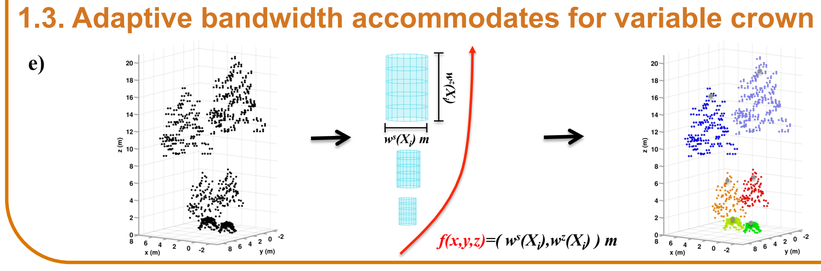

- The lidar point cloud is regarded as a multimodal distribution where each mode, defined as a local maximum both in density and height, corresponds to a single location within the tree crown.
- The modes are calculated according to a 3D Kernel, called bandwidth, that is here represented by a cylinder.
- The bandwidth seeks for the local mode corresponding to each lidar point (**a**).
- The 3D clusters are calculated by gathering the points that had converged towards the same mode (**b**).
- AMS3D is a non-parametric method, i.e. it does not make any assumption regarding the shape of crowns. It is therefore suitable to deal with tropical forests crown shape heterogeneity.
- However, AMS3D is sensitive to crown size and a single bandwidth is not adapted to deal with crown size variability (**c,d**)
- We developed a self-calibrated adaptive bandwidth that accommodates its size to the average crown volume for a given forest height (**e**, Section 2).

2. Method workflow

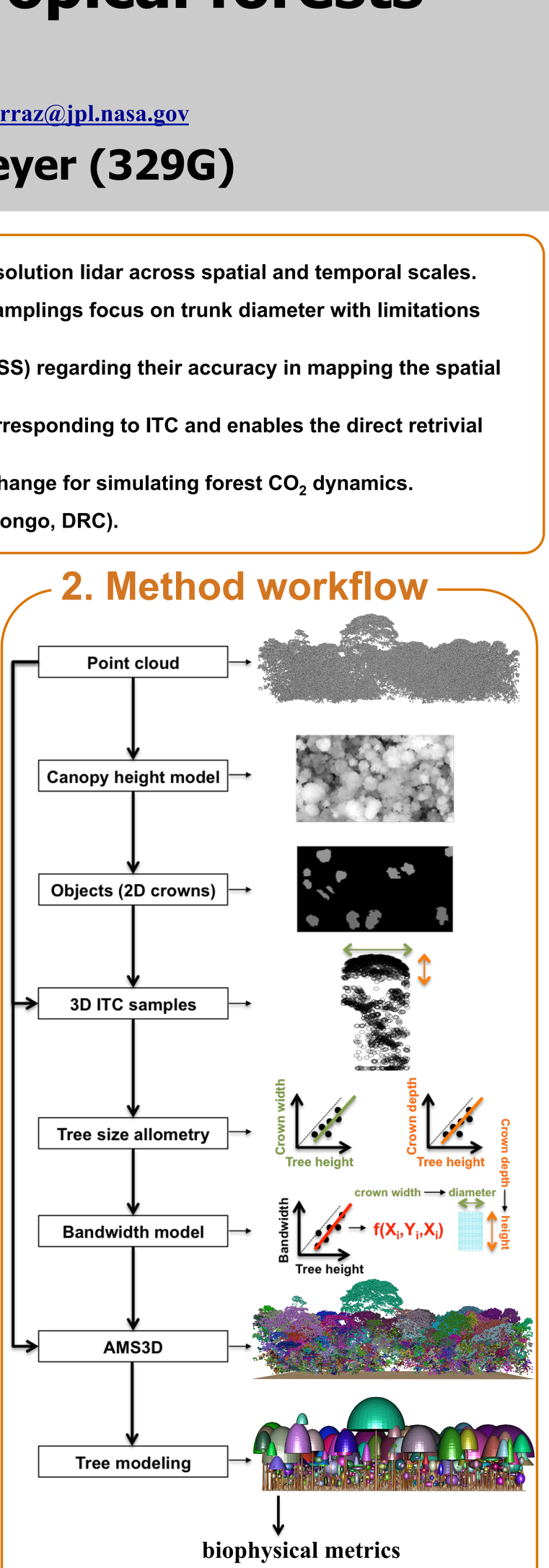

- **tree density**
- **individual tree height**
- **individual crown area and volume**
- **canopy structure profiles**
- **light interception profiles**
- **tree mortality and tree recruitment**

3. Results (examples)

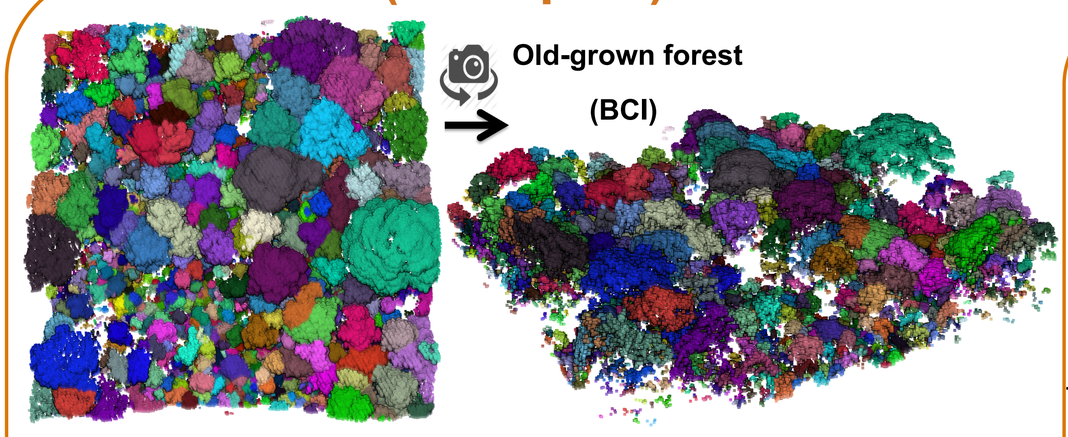

3.1. Biomass estimation

- Aboveground biomass is estimated using **a)** field and **b)** lidar measurements together with an allometric equation [Chave et al., 2015]
- Trunk diameter (**TD**) of individual trees is replaced by crown area (**CA**) in the AMS3D-based model

a) Field-based model

$$AGB = 0.0509 \times \overline{WD} \times \sum_{i=1}^{n} TD_i^2 \times TH_i$$

$\overline{WD}$ =mean wood density TH=tree height

b) AMS3D-based model

$$AGB = a \times \overline{WD} \times \sum_{i=1}^{n} CA_i \times TH_i$$

a =calibration parameter

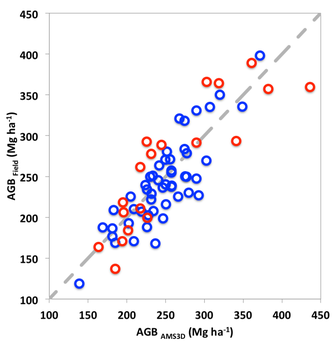

Barro Colorado Island
a=0.96
R^2=0.72
RMSE=28.47 Mg ha^{-1} (11.8%)

Mai Ndombe
a=0.97
R^2=0.75
RMSE=45.40 Mg ha^{-1}(17.9%)

- Results are very satisfactory, indicating that AMS3D has the potential to estimate forest biomass in the absence of field inventory plots.
- The calibration parameter is close to 1 in both study sites, which means that CA is a good proxy for TD.

3.2. Tree density by trunk size class

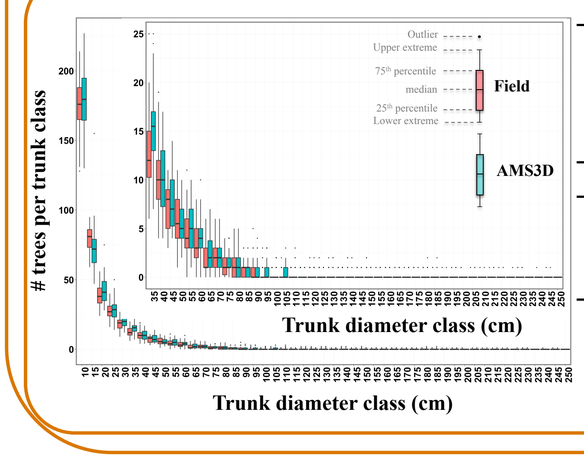

- We converted lidar-derived tree height into trunk diameter to compare results with the field sampling approach.
- Results are for fifty 1ha plots in BCI.
- On average, AMS3D is able to accurately estimate tree density for every trunk diameter class.
- It allows quantifying the variability of relationships among tree size-frequency distributions, biomass and tree density across spatial scales.

Conclusion

- **AMS3D was successfully applied to two tropical forests measured using different lidar point cloud densities. It is a robust approach able to accurately estimate tree density, individual tree height and crown size. Results of ongoing assessments over La Selva (Costa Rica) and Borneo Island (Indonesia) are very satisfactory.**
- **The AMS3D maps cover much larger areas than field samplings and they provide finer scale 3D measurements that better explain the tropical forest structure variability in both vertical and horizontal dimensions.**
- **Information on individual tree size can be used to feed existing biomass allometric equations and generate biomass maps over large and remote areas, which are crucial to calibrate the products delivered by the upcoming NASA spatial missions GEDI and NISAR or the ESA mission BIOMASS.**
- **The fine scale 3D tropical forest structure characterization makes possible the study of vertical vegetation profiles, light conditions, gap dynamics, forest growth , mortality and recruitment over space and time.**

National Aeronautics and Space Administration
Jet Propulsion Laboratory
California Institute of Technology
Pasadena, California

www.nasa.gov

ELSEVIER
Remote Sensing of Environment
Volume 183, 15 September 2016, Pages 318–333

Lidar detection of individual tree size in tropical forests

António Ferraz[a], Sassan Saatchi[b], Clément Mallet[c], Victoria Meyer[b, d]

Poster No. EA-2

National Aeronautics and Space Administration

Quantification of Tropical Forest Biomass and its Changes through Using InSAR Phase Measurements

Postdoc: Yang Lei (335F)
Advisor: Robert Treuhaft (335F)

Introduction

- The status of aboveground biomass (AGB) in tropical forests and its changes are essential in monitoring the carbon budget, and the consequent climate change.
- In this study, the Interferometric Sythetic Aperture Radar (InSAR) phase measurements instead of the widely-used InSAR/PolInSAR (Polarimetric InSAR) complex correlation measurements, are re-examined and utilized to reveal a new estimate of forest-height temporal change.
- This approach has been validated with German Aerospace Center (DLR)'s TanDEM-X (the first spaceborne single-pass InSAR satellite mission) data over ground validation sites in Brazil (where selective logging is known to occur for some stands).
- The approach is capable of measuring the temporal change of tropical forest height (resulting from forest disturbance and regrowth) to a sub-meter accuracy for the first time, which is comparable or even better than the existing InSAR/PolInSAR methods (few-meter accuracy).

Mission Overview

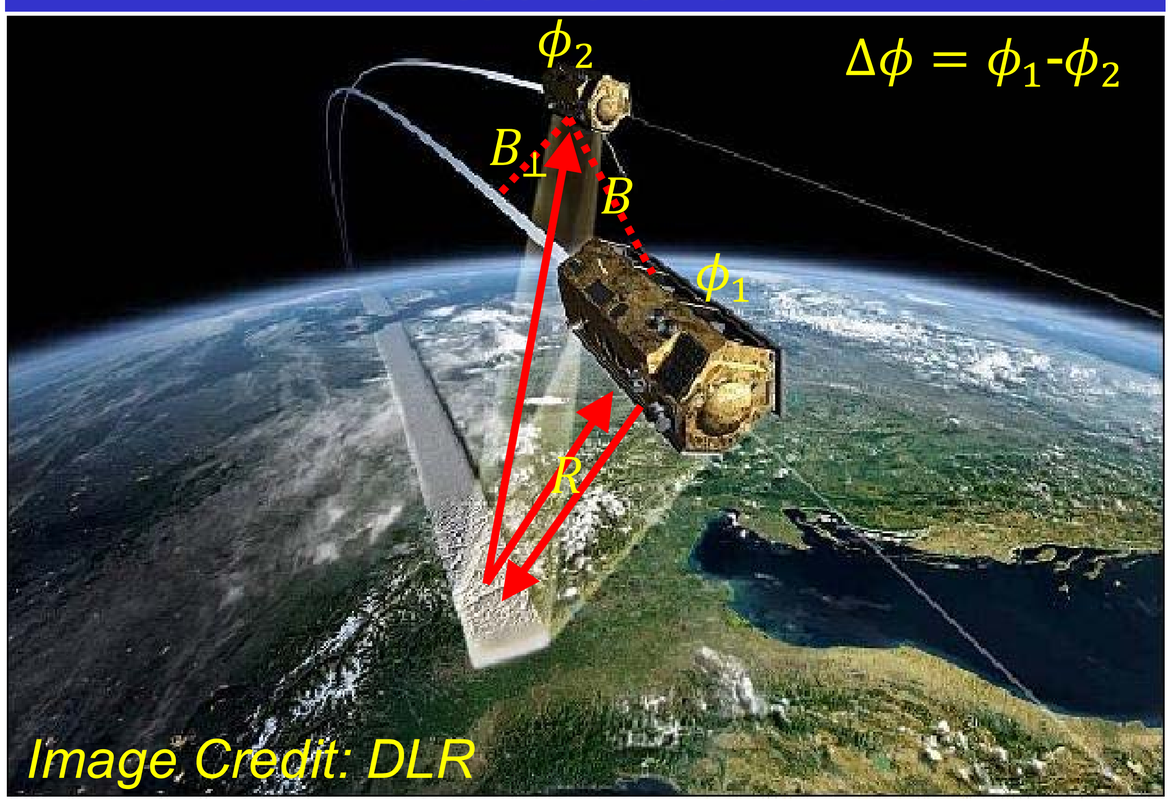

Methodology

Interferometric phase-inverted height $\frac{\Delta\phi}{\kappa_z} = h + const(H)$

Interferometric vertical wavenumber $\kappa_z = \frac{2\pi B_\perp}{\lambda R \sin\theta}$

Time-series of single-pass InSAR observations

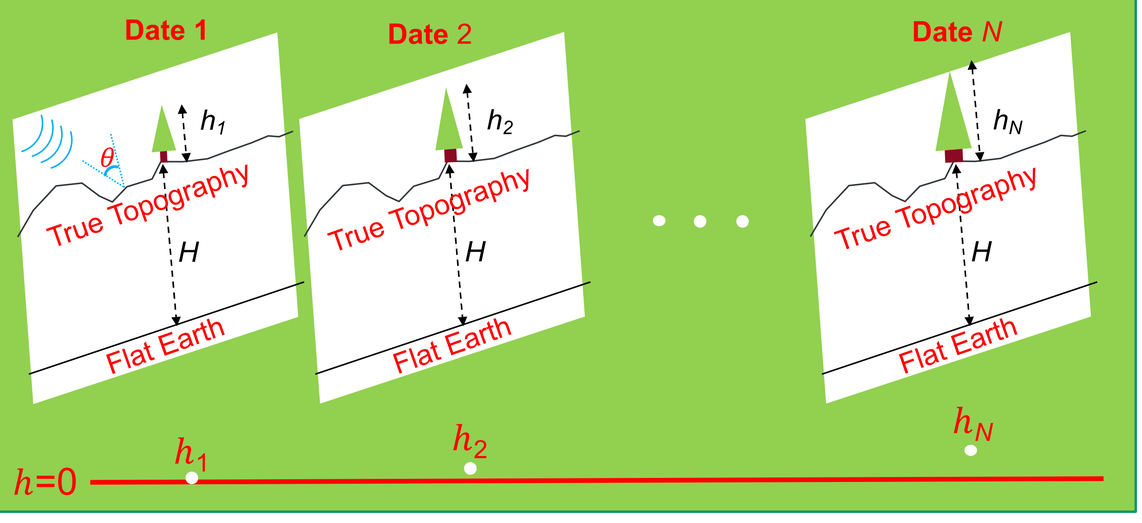

Dataset and Study Area

- 34 InSAR imageries between 2011 and 2014 from TerraSAR-X and TanDEM-X are selected and processed with the flat-earth effects removed.
- The study area consists of 78 50m × 50m stands in Brazil, where field measurements of AGB were collected in 2010 and 2013.

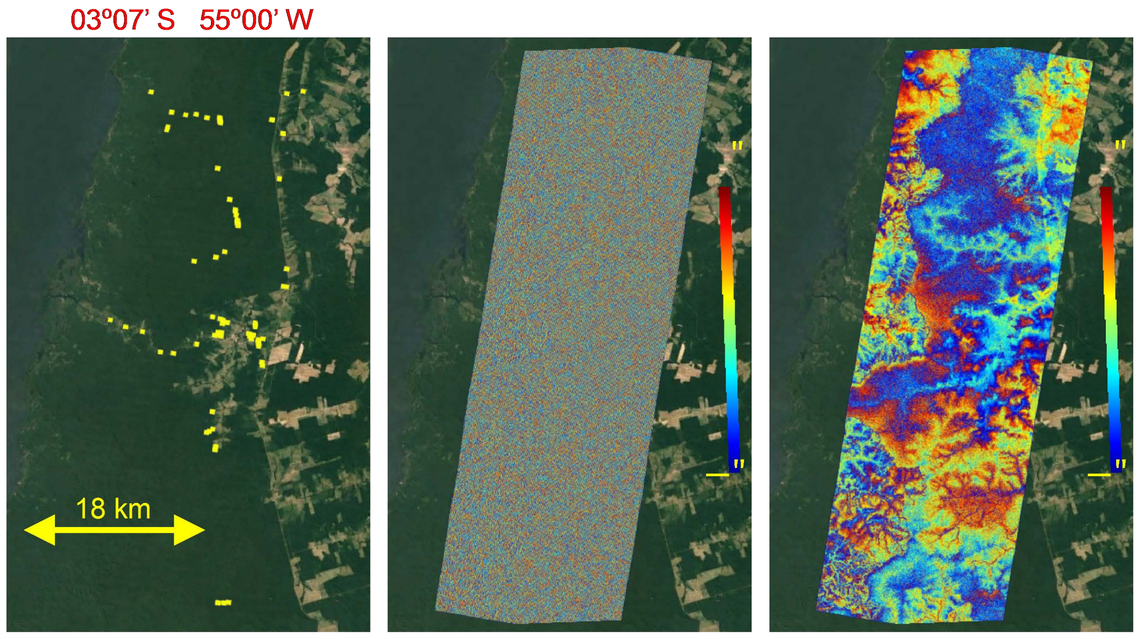

** The yellow dots in the optical image illustrate the location of the 78 test stands.*

Results

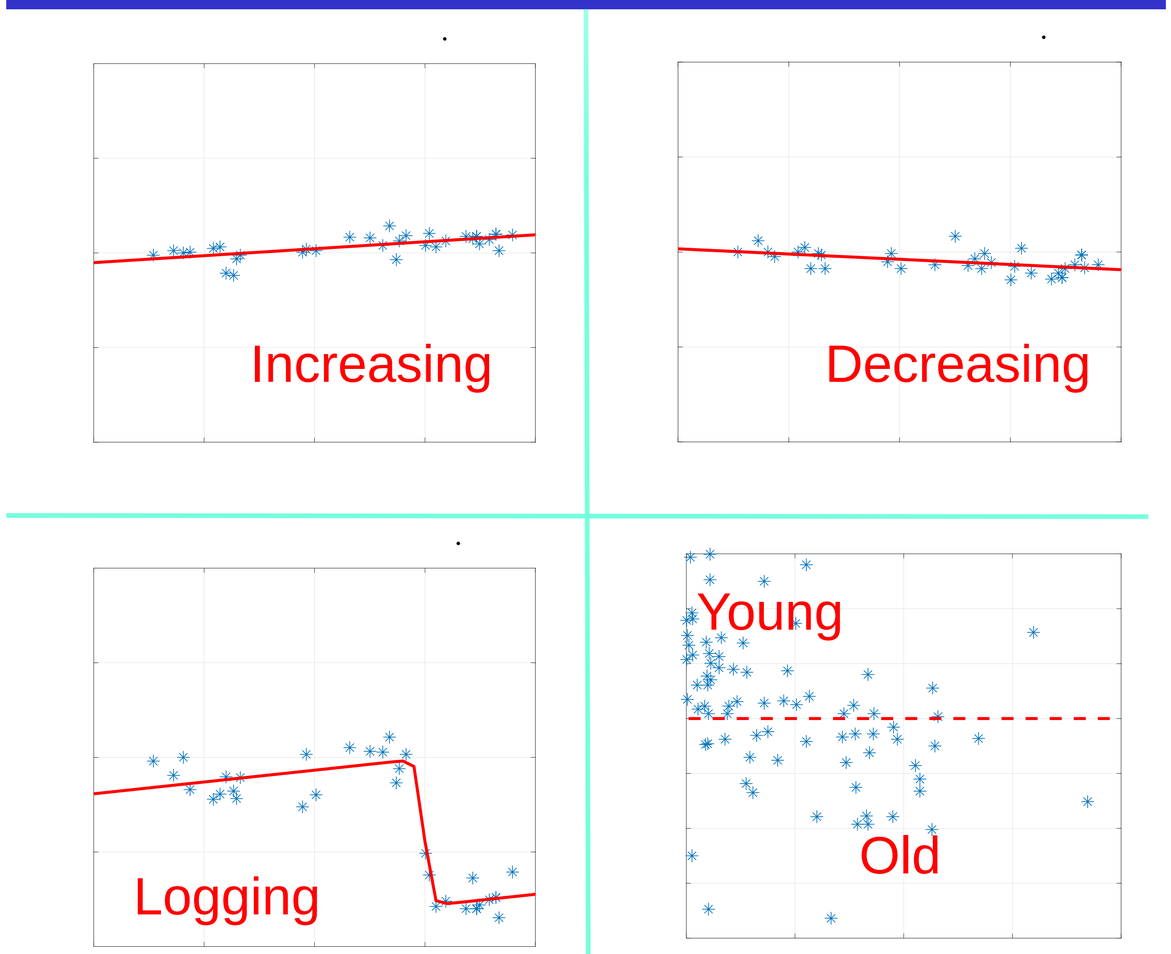

Future Work

The current study cannot measure the absolute value of forest height; rather, it characterizes the change of forest height compared to a reference height. Through utilizing the histogram of the interferometric phase values for all of the pixels within each stand, it is possible to retrieve the absolute value of forest height, which will considerably enhances the above analysis and also serves as a important contribution in its own right.

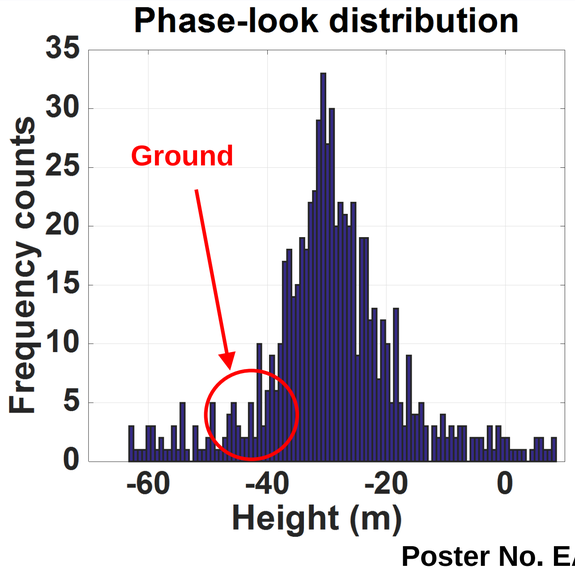

National Aeronautics and Space Administration

Jet Propulsion Laboratory
California Institute of Technology
Pasadena, California

Acknowledgements: This work was supported by an appointment to the NASA Postdoctoral Program at the NASA Jet Propulsion Laboratory, administered by Universities Space Research Association under contract with NASA.

www.nasa.gov

Poster No. EA-3

National Aeronautics and Space Administration

Warming trends and heatwave dynamics over the LA region using a new MODIS Land Surface Temperature (LST) product

Nabin K Malakar (329-G) and Glynn C Hulley (329-G)

Summary

- A new NASA Land Surface Temperature and Emissivity (LSTE) product (MOD21) developed at JPL is used to investigate spatiotemporal characteristics of surface temperatures over LA.
- MOD21 LST data from 2003-2016 reveal an average warming trend of 1.3°C per decade (up to 1.6 °C) over urban LA regions.
- An increase in heatwave duration, frequency, and nighttime temperatures is observed during the 1950-2016 period.
- MOD21 LST data during severe heatwave events reveal that lower-income neighborhoods are at the greatest risk.
- This information can be used for more efficient allocation of resources and more effective adaption and mitigation techniques during extreme temperatures by decision makers.

MOD21: A New NASA LSTE Product

- The MODIS suite of thermal sensors onboard the Terra and Aqua platforms observe Earth twice daily at 1-km nadir resolution.
- **A new standard NASA LSTE product (MOD21) conceived and developed at JPL,** will be released to the public as collection 6 during 2016.
- While previous products (MOD11) have relied on the fixed emissivity assumption, MOD21 physically retrieves the LST&E making it more suitable for urban studies.
- MOD21 LST has an accuracy of ~1 K over all surface types.

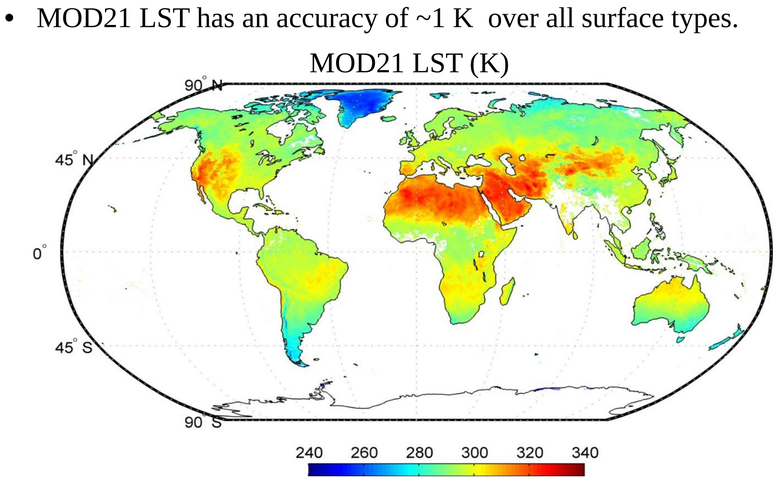

Figure 1. MOD21 Average Land Surface Temperature (LST) for August 2004.

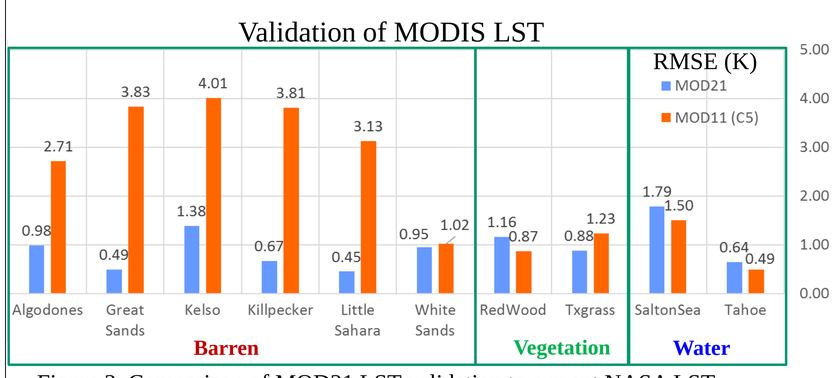

Figure 2. Comparison of MOD21 LST validation to current NASA LST (MOD11) over various surface types using three years of data show that MOD21 retrieves LST consistently with accuracy of ~1K.

Study Area: Los Angeles, CA

Data:

- MOD21 granules covering LA processed locally at JPL
- Entire archive of MODIS lifetime data (2003-2015) was processed.
- Data over each region was extracted with strict quality control.

Quality Control:

- View angle < 45°
- Emissivity at bands 31 and 32 > 0.95
- Precipitable Water Vapor < 4cm
- Clouds screened and extended

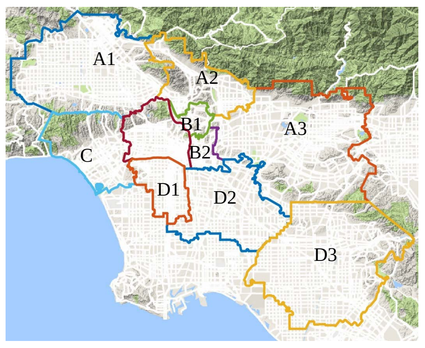

Figure 3. For our initial study, the LA region is divided into four zones
A: Foothills/Valley
B. Downtown LA
C. Coastal LA
D. South LA
These regions will be further expanded and revised in the future.

National Aeronautics and Space Administration

Jet Propulsion Laboratory
California Institute of Technology
Pasadena, California

www.nasa.gov

Poster No. EA-4

Land Surface Temperature Warming Trends over LA

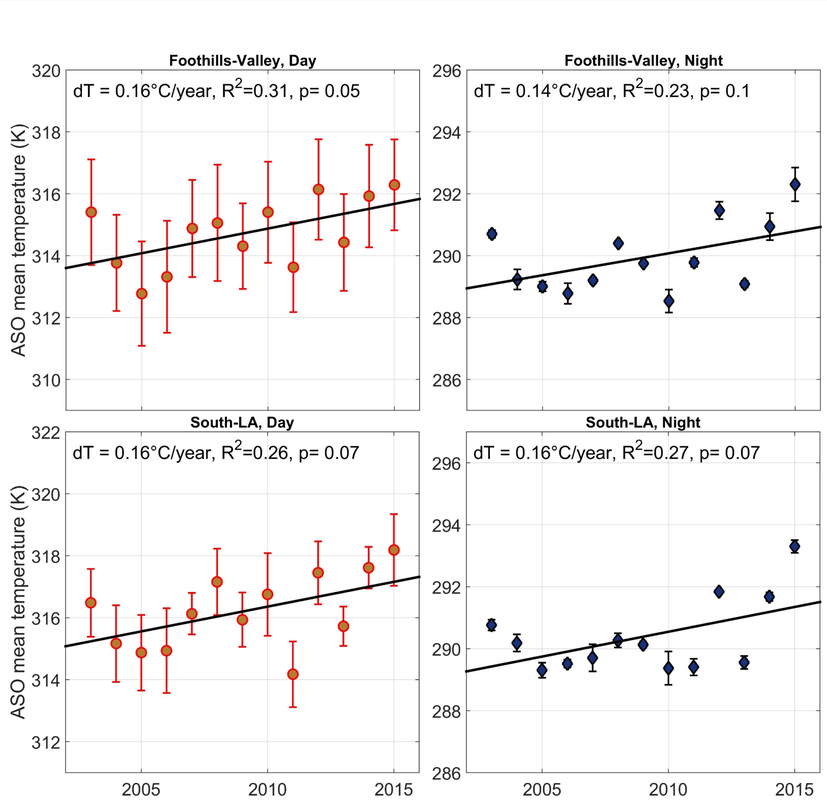

Figure 4. Mean day and nighttime LST trends for Aug-Sep-Oct show warming trends over Valleys and South LA of up to 1.6 degree per decade for both day and night.

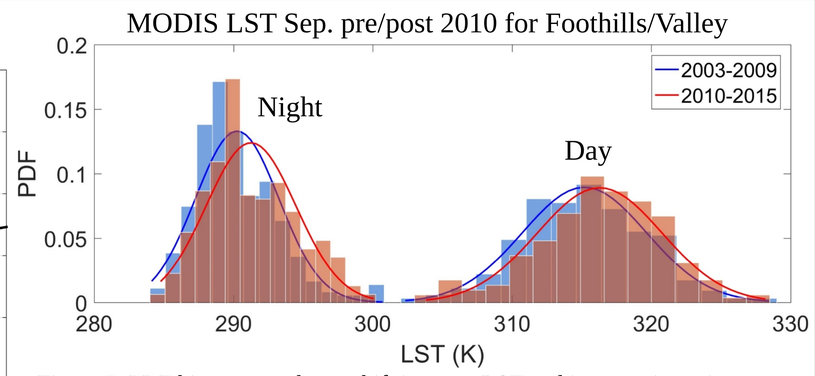

Figure 5. PDF histograms shows shift in mean LST and increase in variance before and after 2010, for the month of September.

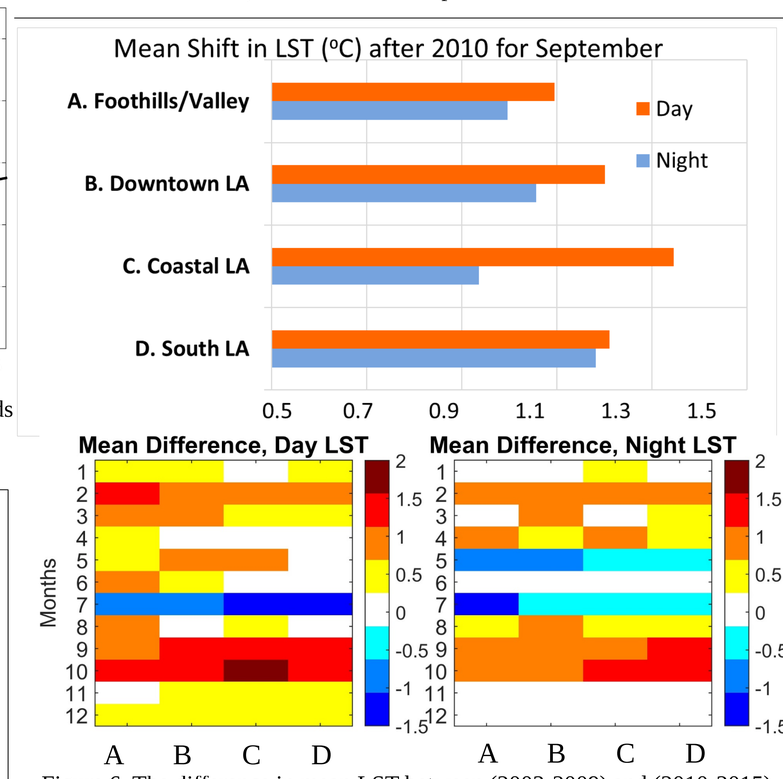

Figure 6. The difference in mean LST between (2003-2009) and (2010-2015) for four LA regions for both day and night LST. The relative cooling in July needs further investigation but could be attributed to a strong La Nina in 2011.

Result 1. Summer/Fall average LST show strong warming trend

- Warming trends of up to 1.6° per decade for both day and night time retrievals over all regions investigated.
- Average daily warming rate is about 1.3 °C per decade for the entire LA region.

Result 2. A shift towards warmer mean LST and larger variance

- The mean daily LST has increased by more than 1 °C during past five years when compared to 2003-2010 baseline.
- This combined with an increase in variance will lead to a dramatic increase in record hot weather as illustrated in next section.

More Frequent and Longer Lasting Heatwaves Over LA

Heatwave definition and detection:

- A period of at least 3 days or more where combined effects of excess heat and heat stress are unusual with respect to climatology.
- Both day (maximum) and night (minimum) temperatures are used. The Excess Heat Index (EHI) is defined as:

$$EHI = T_i - T_{97.5} \qquad T_i = (T_{max} + T_{min})/2$$

$$T_{97.5} = 97.5^{th}\ percentile\ of\ daily\ T_i\ climatology$$

- Using air temperature data from the NCDC station network in LA we analyzed temporal variation of heatwaves from 1950 – 2016.

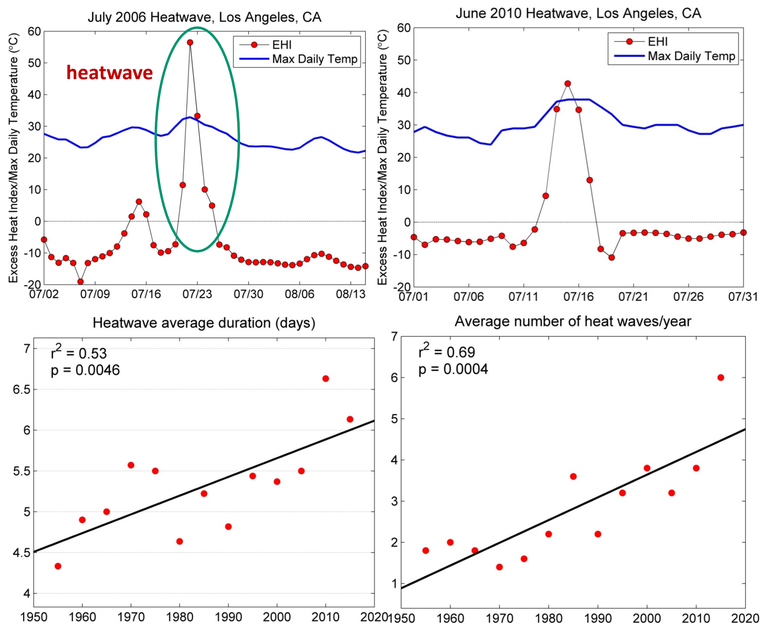

Figure 7. Heatwave detection using EHI (top), and trends in heatwave duration and frequency (bottom).

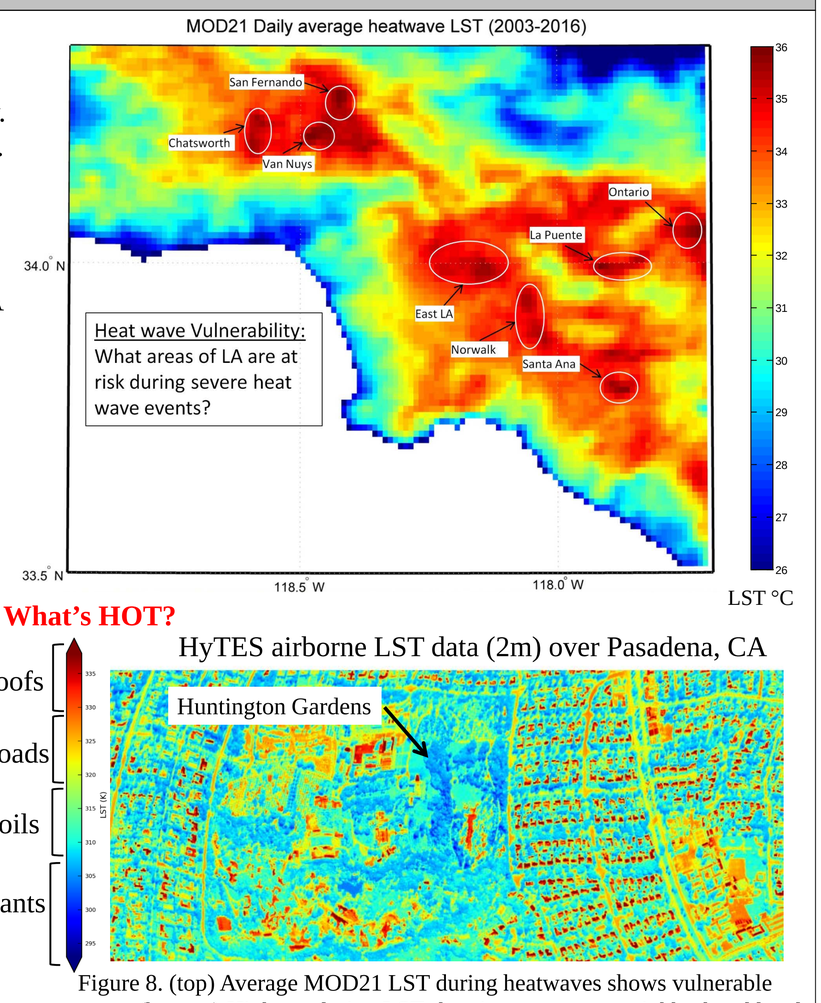

Figure 8. (top) Average MOD21 LST during heatwaves shows vulnerable areas. (bottom) High-resolution LST showing patterns at neighborhood level.

The Road Ahead

- Study regions in LA will be refined to exclude vegetated regions and include coastal regions paying attention to ocean pixel screening
- Study domain will be extended to include other major US cities such as Chicago, Phoenix, and Washington DC.
- MOD21 LST time series (2003-2016) will be used to investigate warming trends and spatial patterns, while NCDC local air temperature data will be used to detect heatwaves and develop a temporal heatwave climatology for each major US city
- The socio-economic impacts of increasing temperatures and heatwaves will be assessed for specific LA neighborhoods.

National Aeronautics and Space Administration

In Situ Carbon Dioxide and Methane Measurements from a Tower Network in Los Angeles

Lead Author: Kristal R. Verhulst (329G)

Co-Authors: A. Karion (NIST), J. Kim (SIO), V. Yadav (398L), T. Pongetti (329H), P. Salameh (SIO), C. Wong (329H), P. Rao (329G), F. Hopkins (329G), K. Mueller (NIST), C. Sloop (Earth Networks), S. Newman (Caltech), J. Miller (NOAA/ESRL/CIRES), R. F. Weiss (SIO), R F. Keeling (SIO); C Miller (329G); and R. Duren (8000)

1. Introduction

- A disproportionate fraction of resources and fossil fuels are consumed in megacities – metropolitan areas with populations >10 million – concentrating fossil-fuel related greenhouse gas (GHG) emissions into a small fraction of earth's land surface.
- The Megacities Carbon Project is a multi-national, multi-institution project aimed at measuring GHG emissions from large urban areas. Here we report CO_2 and CH_4 measurements in the Los Angeles (LA) Megacity during 2013-2016.
- We discuss urban GHG measurement strategies, signals of interest for urban studies, analytical uncertainty estimates. We also show initial estimates of the GHG enhancements in LA and estimate CH_4 emissions in LA using tracer:tracer correlations.

2. Objectives

(1) Measure CO_2 and CH_4 and calculate time-dependent analytical uncertainty estimates

(2) Estimate local background mole fractions and enhancements above background

(3) Use tracer:tracer ratios and CO_2foss from 14C measurements to estimate emissions

3. Carbon Dioxide and Methane Observations

- There are generally 3 signals of interest for urban GHG studies, all of which are relevant for inverse modeling studies:

(1) Diurnal patterns: Changes at one location within 24-hour period
(2) Gradients: Mole fraction difference between locations within network
(3) Local enhancement: $X_{excess} = X_{obs} - X_{BG}$

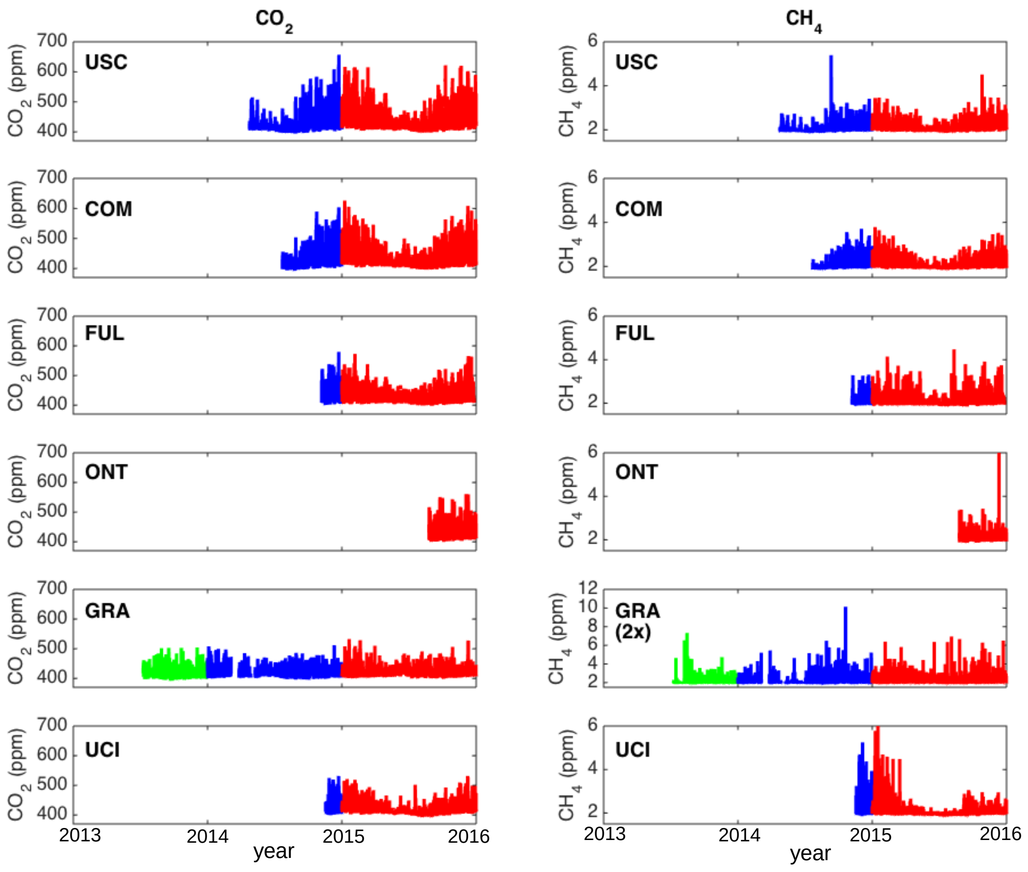

4. Time-dependent Analytical Uncertainty Estimates

Uncertainty in enhancements:

$(U_{excess})^2 = (U_{air})^2 + (U_{BG})^2$

Analytical uncertainty:

$(U_{air})^2 = (U_M)^2 + (U_{ex})^2 + (U_{h2o})^2$

where:

$U_M = U_{TGT}$

or

$(U_M)^2 = (U_p)^2 + (U_b)^2 + (\sigma_{sc})^2$

whichever is larger.

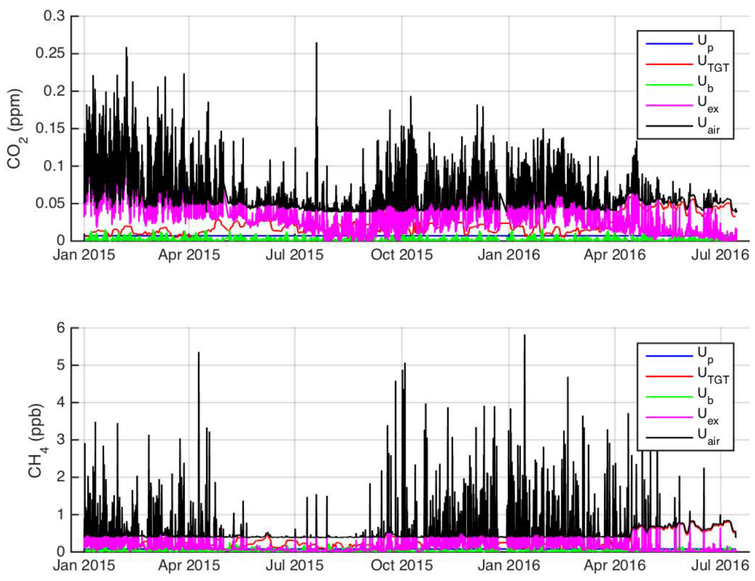

- Overall U_{ex} is the largest component of the analytical uncertainty (U_{air}). U_{excess} is dominated by background uncertainty. Both U_{air} and U_{BG} will ultimately translate to uncertainty in flux estimates.

5. Estimating CO_2 and CH_4 Enhancements in LA

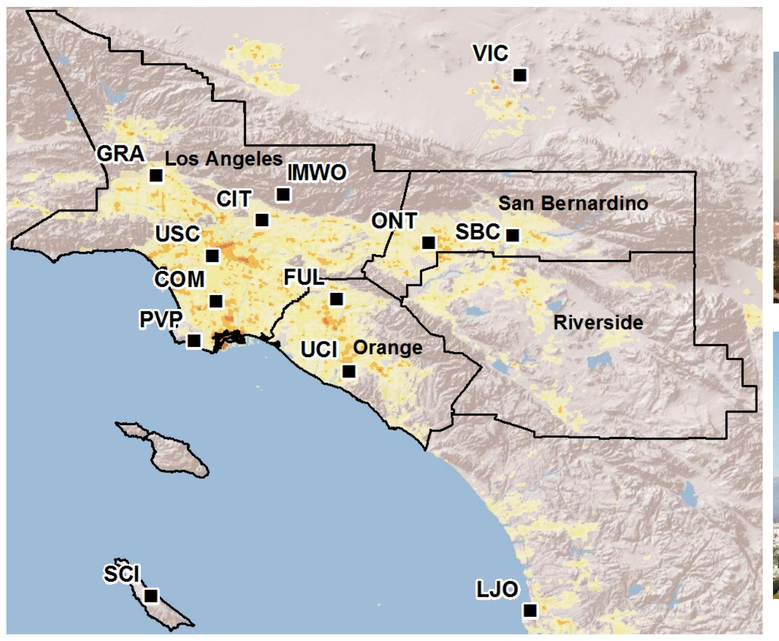

Background Estimates

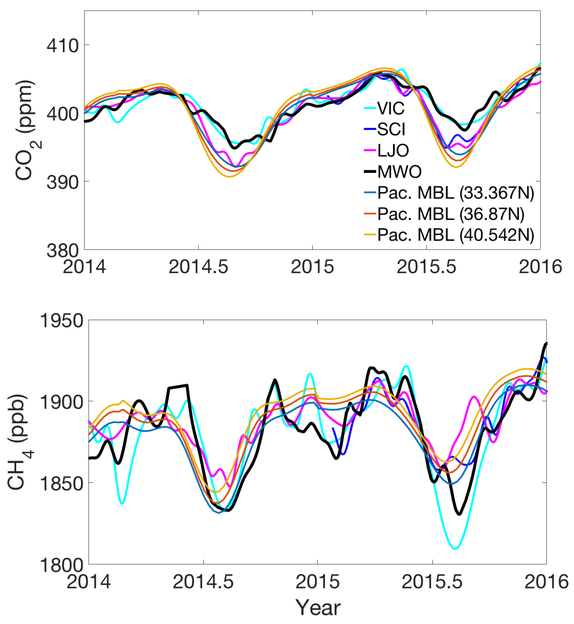

Monthly Average Enhancements

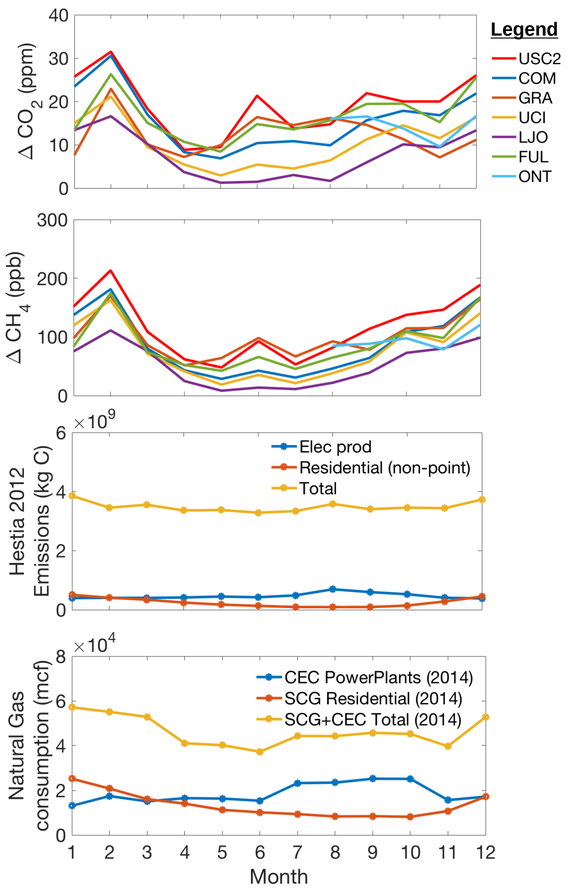

- Observations from the VIC, SCI, and LJO sites were used to estimate background and calculate CO_2 and CH_4 enhancements
- Monthly average CO_2 and CH_4 enhancements show a peak in winter; smaller peak in summer, following fossil fuel carbon emissions patterns and NG consumption data (Hestia 2012 and Wong et al., 2016)

6. Estimating CH_4 emissions using CO_2fos (from ^{14}C)

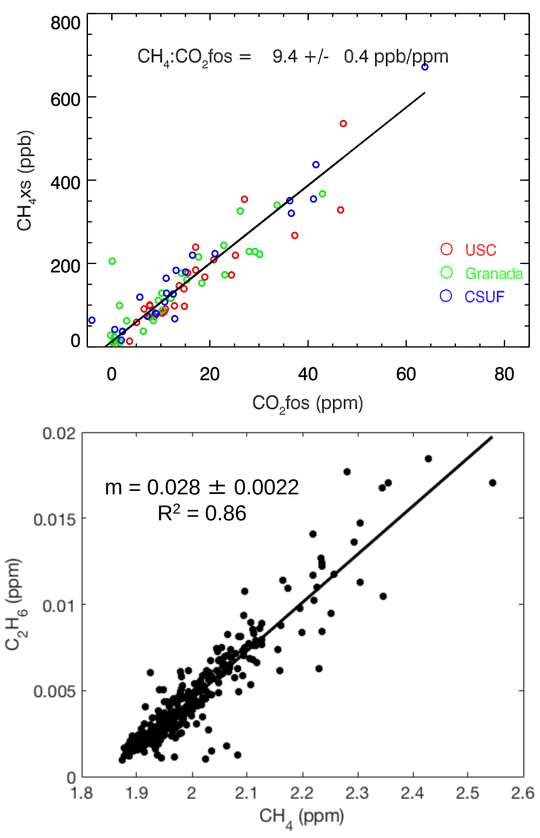

- Assume CO_2 emissions for LA are known, and approximate CH_4 emissions as:

$$E_{CH_4}^{LA} = \left(\alpha_{CH_4} \frac{M_{CH_4}}{M_{CO_2}}\right) E_{CO_2}^{LA}$$

$E_{CH_4}^{LA}$ = 267.6 ± 11.4 Gg CH_4/y

- Scaling up for the South Coast Air Basin (based on population):

$$E_{CH_4}^{SCB} = 267.6\ Gg \frac{CH_4}{y} * \left(\frac{0.43}{0.27}\right)$$

$E_{CH_4}^{SCB}$ = 426.3 Gg CH_4/y

- C_2H_6:CH_4 similar to that of natural gas based on flasks from 3 sites (see e.g. Conley et al., 2016)

Future work:

- Time-dependent selection of background observations based on winds
- Inverse modeling of CO_2fos and CH_4 in SoCAB
- Use tracers (^{14}C flask observations and continuous CO) to provide continuous CO_2fos estimates
- Continuous monitoring of C_2H_6:CH_4 using a new Aerodyne analyzer installed at the GRA site

National Aeronautics and Space Administration

Jet Propulsion Laboratory
California Institute of Technology
Pasadena, California
www.nasa.gov

Acknowledgements: Special thanks to my supportive colleagues and advisors at JPL, NIST, NOAA, and SIO. This project is jointly funded by the US National Aeronautics and Space Administration (NASA), National Institute of Standards and Technology (NIST) GHG and Climate Science Measurements Program, and National Oceanographic and Atmospheric Administration (NOAA). This work would not be possible without technical support for the methods, instrumentation, and software from: the National Institute of Standards and Technology (NIST), Scripps Institution of Oceanography, GCWerks, and Earth Networks (Christopher Sloop, Clayton Fain, Donnie Bixler, Steve Prinzivalli, and Bill Angel). Government sponsorship acknowledged.

Poster No: EA-5

National Aeronautics and Space Administration

Spectral dependence of solar-induced chlorophyll fluorescence: Implications for space-borne measurements of OCO-2 SIF

Author: Troy Magney (329G)

Christian Frankenberg (Caltech), Joshua Fisher (329G), Ying Sun (329G), Gretchen North (Occidental), Thomas Davis (Cal Poly)

Introduction:

- Recent advances have been made in the retrieval of solar-induced **chlorophyll fluorescence (SIF)** from space and could provide a **significant step towards mapping instantaneous plant photosynthesis across space and time**.
- While these advances are promising, there are still many **unresolved issues** related to the spatial, spectral, and temporal scale-change problem, making **interpretation of the mechanisms driving the SIF signal** from space challenging.

Global SIF as a proxy for photosynthesis?

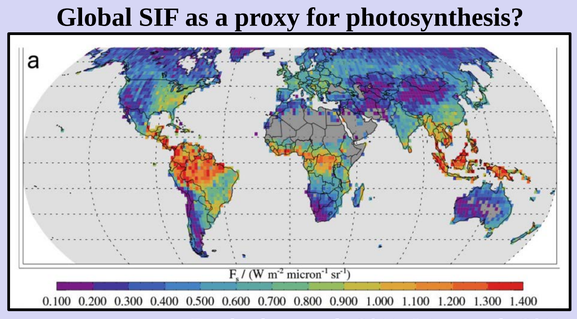

Frankenberg et al., 2011; Joiner et al., 2011

What does chlorophyll do with absorbed photosynthetically active radiation?

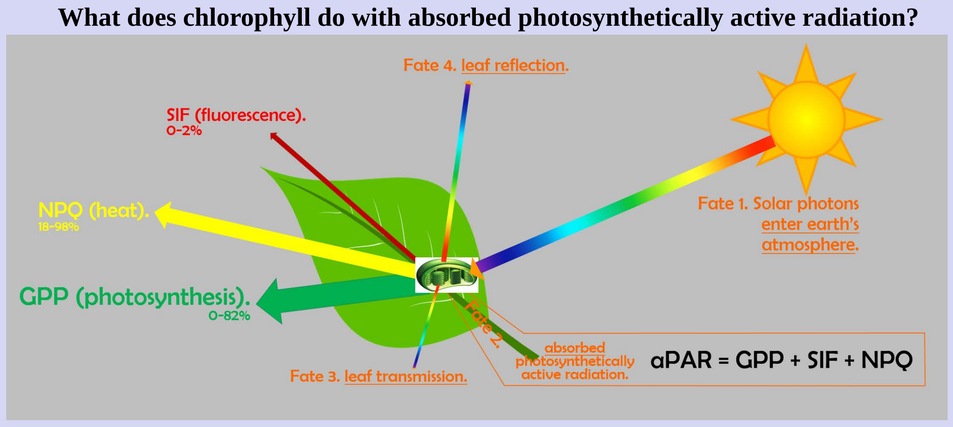

Problem:

- Decades of research into the relationship between fluorescence and photosynthesis
- Active fluorescence (PAM) measurements use a broad band integral ~ 700 nm- 850 nm

Knowledge gap relating spectral SIF to photosynthesis

- Recent global retrievals of SIF from GOSAT, GOME-2, OCO-2 show strong correlations to GPP
- However, SIF measurements are passive, and therefore can only assess wavelength dependent SIF

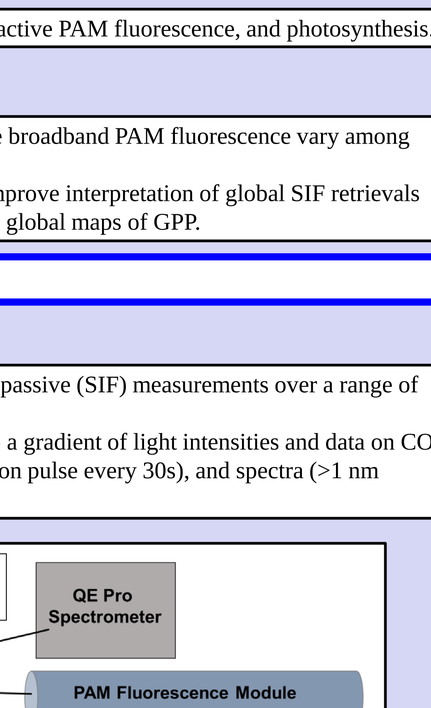

KISS fluorescence workshop, 2012

Primary Objective:

- Advance our understanding of the relationships between passive SIF, active PAM fluorescence, and photosynthesis.

Questions:

- How do the spectrally dependent relationships between SIF and active broadband PAM fluorescence vary among species, stress conditions, pigment content in space and time?
- How can our understanding of leaf and canopy level SIF be used to improve interpretation of global SIF retrievals from GOME-2, GOSAT, and OCO-2 towards providing instantaneous global maps of GPP.

Methods:

- Collect simultaneous measurements of steady-state active (PAM) and passive (SIF) measurements over a range of species under 'stressed' and 'un-stressed' conditions at the leaf scale.
- Run traditional 'light-response' curves, whereby the leaf is exposed to a gradient of light intensities and data on CO_2 and H_2O gas-exchange (every 5 seconds), PAM fluorescence (saturation pulse every 30s), and spectra (>1 nm resolution at .2s with 10 ms integration time) are recorded.

Fig. 1. Schematic for instrument used to measure passive SIF, active fluorescence, and photosynthesis simultaneously

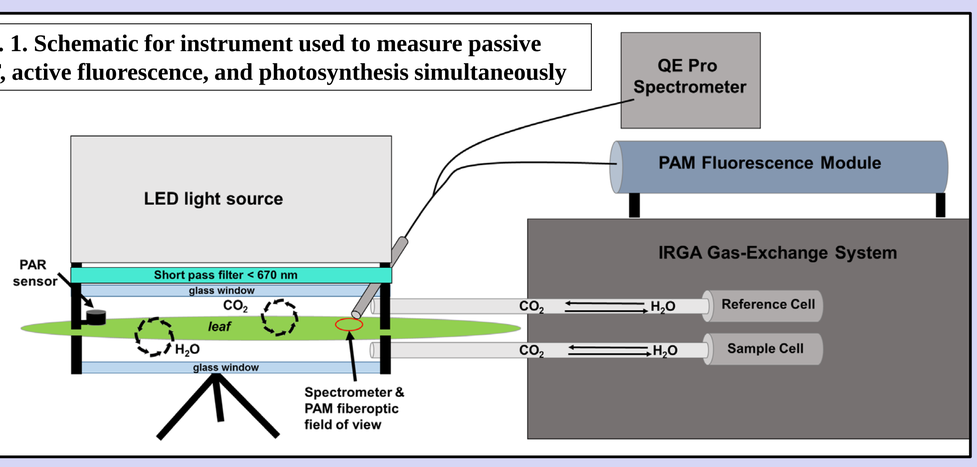

Wavelength dependency of SIF under increasing light:

- Fig. 2a, and c represent a maple leaf exposed to a light response curve under **'non-stress' conditions** (25º C; 20000 ppm H_2O); whereas Fig. 2b, and d represent the same maple leaf (same field of view) under **'stressed conditions'** (40º C; 10000 ppm H_2O) all else being equal.
- **A dampened SIF signal** was observed across all wavelengths between the 'stressed' and 'un-stressed' maple, with **little difference in spectral shape** observed between the two.
- The observed dampening of the SIF signal across all wavelengths in the 'stressed' leaf **corresponds to the photosynthesis data** observed in the corresponding panels in c and d.

Fig. 2.

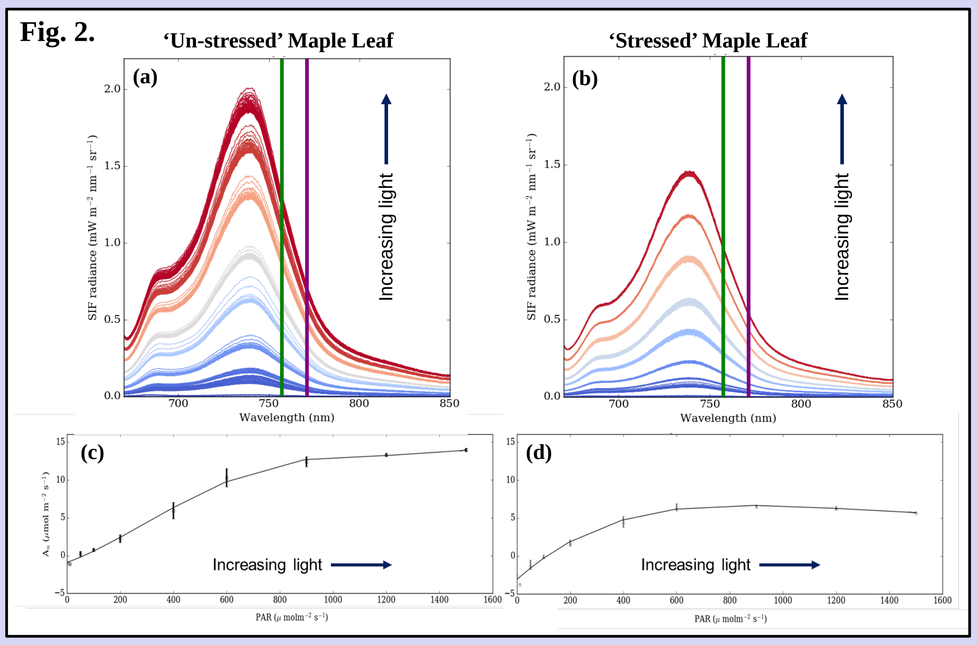

Singular value decomposition of SIF spectra:

- 18 soybean plants were subjected to three different water regimes and ran through light-response curves which **produced different maximum photosynthetic capacities** shown in the legend in subplot A.
- In the first PCA (Fig. 3a), soy plants with lower photosynthetic capacities showed **increased re-emission around the first peak at 686 nm** and **decreased re-emission the second peak at 740 nm.**
- PCA 2 (Fig. 3b) highlights the sensitivity in the first hump, which is primarily driven by differences in **Chl re-absorption.**
- In the wavelengths used by **OCO-2 SIF there was nominal difference** observed in any of the PCAs.

Fig. 3. Wavelength dependent response of SIF

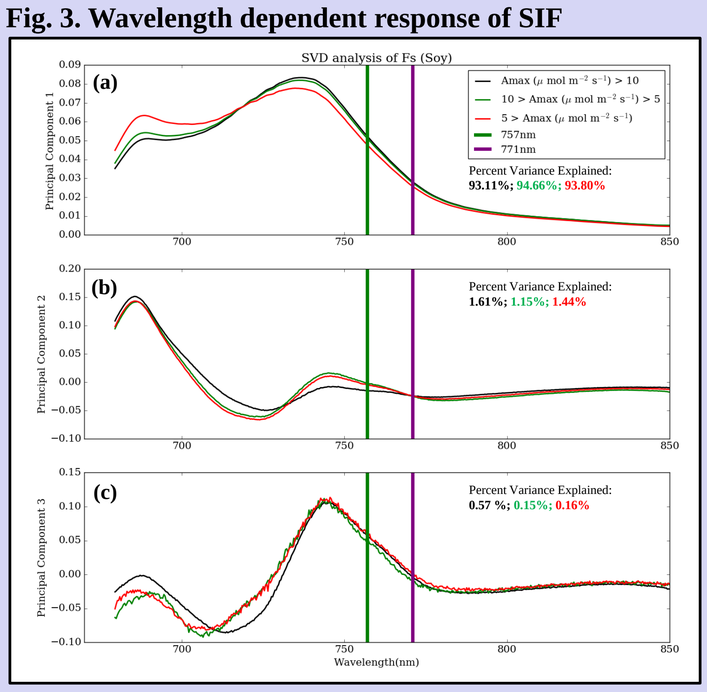

Implications for scaling to OCO-2 SIF:

An **improved understanding of the driving mechanisms behind the SIF** signal could help interpretation of global SIF retrievals though answering several key questions:

1) To what extent is the SIF-GPP relationship driven purely by aPAR? How does it break down under stress?
2) How does the SIF signal observed at the 1:30 pm overpass time of OCO-2 differ from an AM overpass?

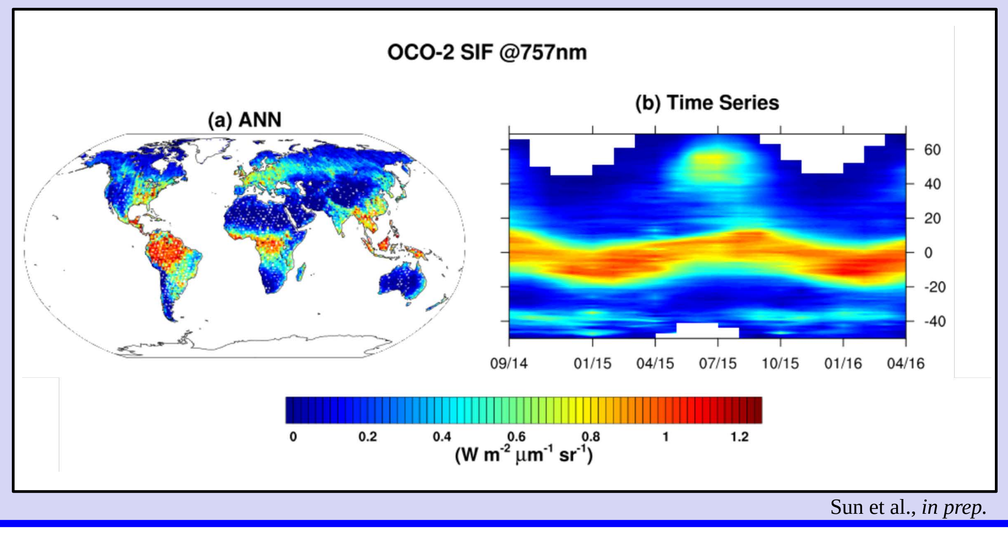

Sun et al., *in prep.*

National Aeronautics and Space Administration

Jet Propulsion Laboratory
California Institute of Technology
Pasadena, California

Acknowledgements:

This work was supported by a NASA Postdoctoral Program Fellowship awarded to TSM, and the Keck Institute for Space Studies. In addition to the co-authors, thanks goes out to Katja Grossman, Jochen Stutz, Darren Drewry, Joe Berry, and Ari Kornfield for helpful insights and discussions. Future work and analysis will be done at the leaf scale under different growing conditions and a wider range of species, in addition to a scaling component including airborne and tower based.

www.nasa.gov

Poster No. EA-7

National Aeronautics and Space Administration

Monitoring Mangrove Forests With UAVSAR

Michael Denbina (334F)
Marc Simard (334F)

Introduction

•Mangrove forests represent some of the most productive ecosystems on Earth. Important areas for conservation and study.

•Very susceptible to sea level rise and human development due to their coastal locations. Disappearing at fast rates.

•In many areas, information on mangrove forest height and biomass is limited, and with high uncertainty.

•We are using data from NASA's Uninhabited Aerial Vehicle Synthetic Aperture Radar (UAVSAR) instrument to map mangrove forest heights across a number of study areas in South America.

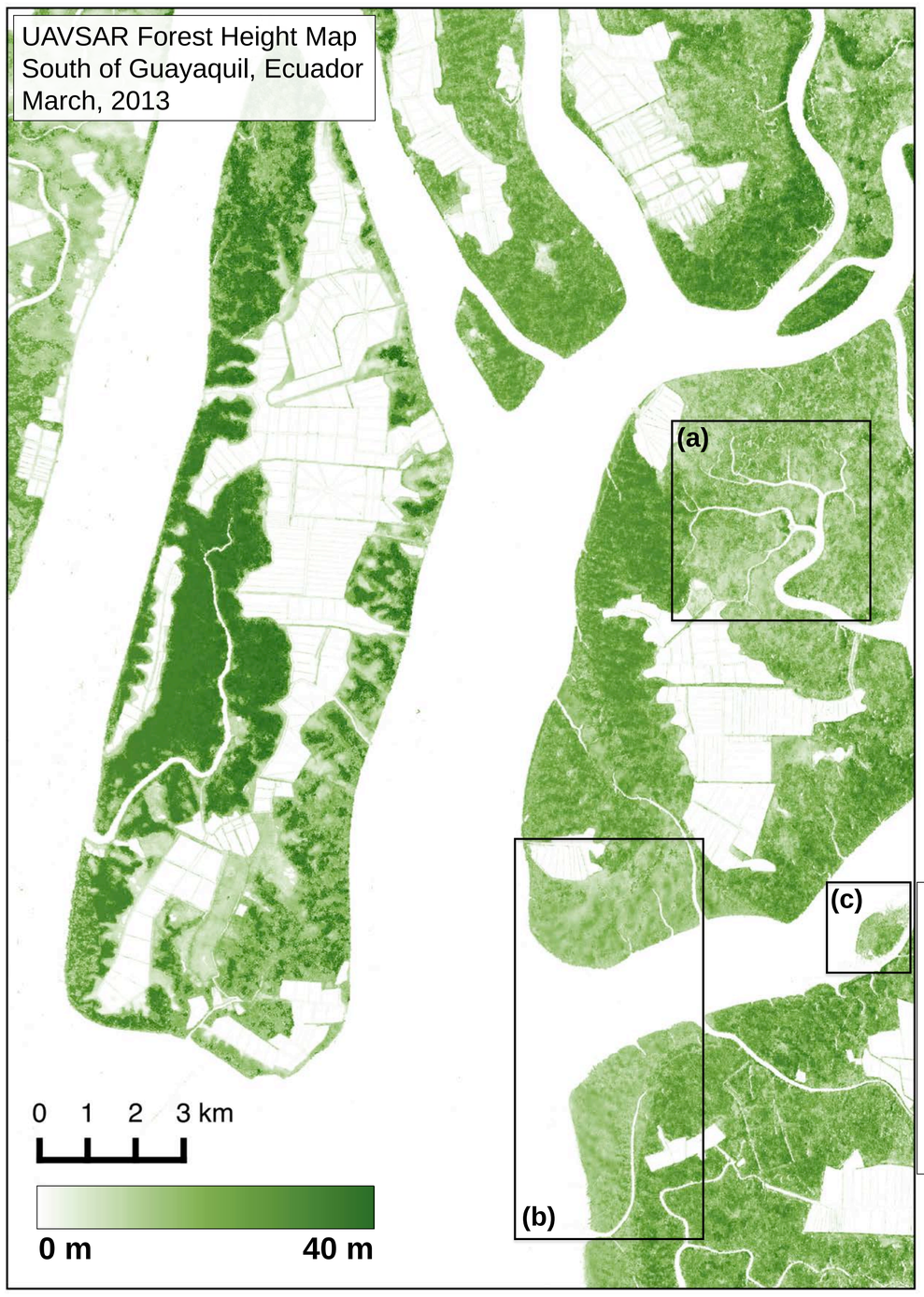

(a) Clear delineation of small rivers and other fine scale features.
(b) New growth since SRTM acquisition.
(c) Island not visible in SRTM.

Methods

- Repeat-pass polarimetric interferometry using UAVSAR data.
- Shuttle Radar Topography Mission (SRTM) elevation data used to help guide the forest model inversion, and compensate for the effect of temporal decorrelation on the UAVSAR data.

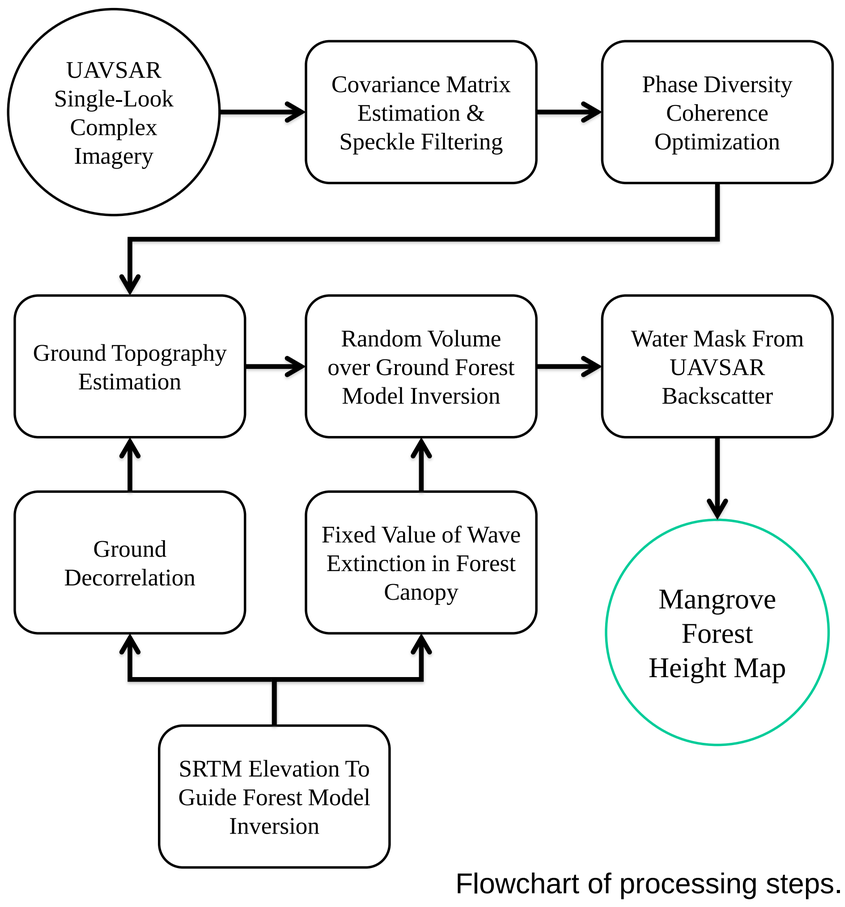

Flowchart of processing steps.

UAVSAR Forest Heights vs. Field Data (Ecuador)

Conclusions

•**Produced UAVSAR-derived forest height maps for areas in Ecuador and Colombia**. Ecuador map validated using field plots (2.76 m RMS error, $r^2 = 0.95$). For Colombia area, no field data available.

•**Proof of concept for fusion of UAVSAR and SRTM data**. Helps compensate for temporal decorrelation effects which introduce a bias into the UAVSAR forest height estimates if not accounted for.

•**Results are higher resolution and more recent than SRTM**. Details are visible in the UAVSAR maps which are not present in the SRTM (small rivers, and recent forest growth). Wider coverage area than is possible with field data.

•**Next Steps**: Refine method and apply to UAVSAR data for other study areas in Costa Rica and Colombia. Use forest height maps to estimate above-ground biomass. Measure mangrove growth/loss using UAVSAR data from multiple years (data was collected in both 2013 and 2015).

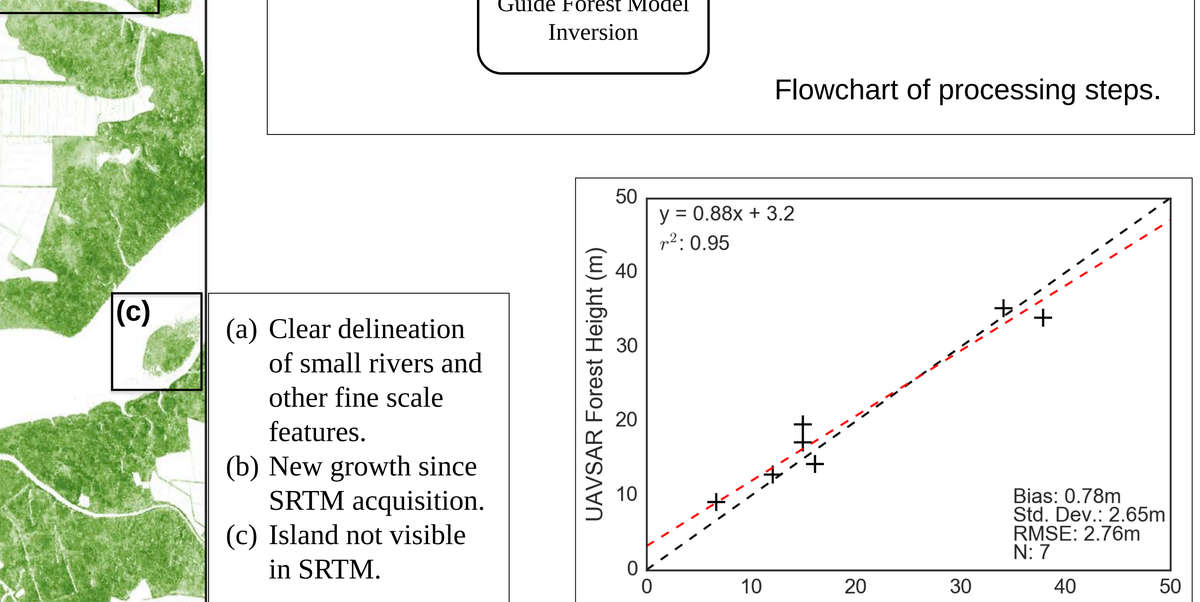

National Aeronautics and Space Administration

Jet Propulsion Laboratory
California Institute of Technology
Pasadena, California

www.nasa.gov

Poster No. EA-8

National Aeronautics and Space Administration

Antarctic Ice Sheet Grounding line migration monitoring using very short repeat-time SAR Interferometry

Pietro Milillo (334)
Eric Rignot (334), Bernd Scheuchl, Jeremie Mouginot, Xin Li (UC Irvine)

Rationale

The grounding line marks the transition zone where ice detaches from the bed and becomes afloat in the ocean.
Prior attempts of grounding lines mapping have been limited because few space-borne SAR missions offer the short-term repeat pass capability required to map the differential vertical displacement of floating ice at tidal frequencies with sufficient detail to resolve grounding line boundaries in areas of fast ice deformation.
We are taking advantage of data being acquired by the Italian COSMO-SkyMed (CSK) mission, a constellation of 4 second generation X-band SAR satellites capable of collecting data with short repeat orbits (1,3,4 days), to monitor the characteristics of grounding line migration using very short repeat-time interferometry in the West Antarctic Ice Sheet (WAIS) sector.

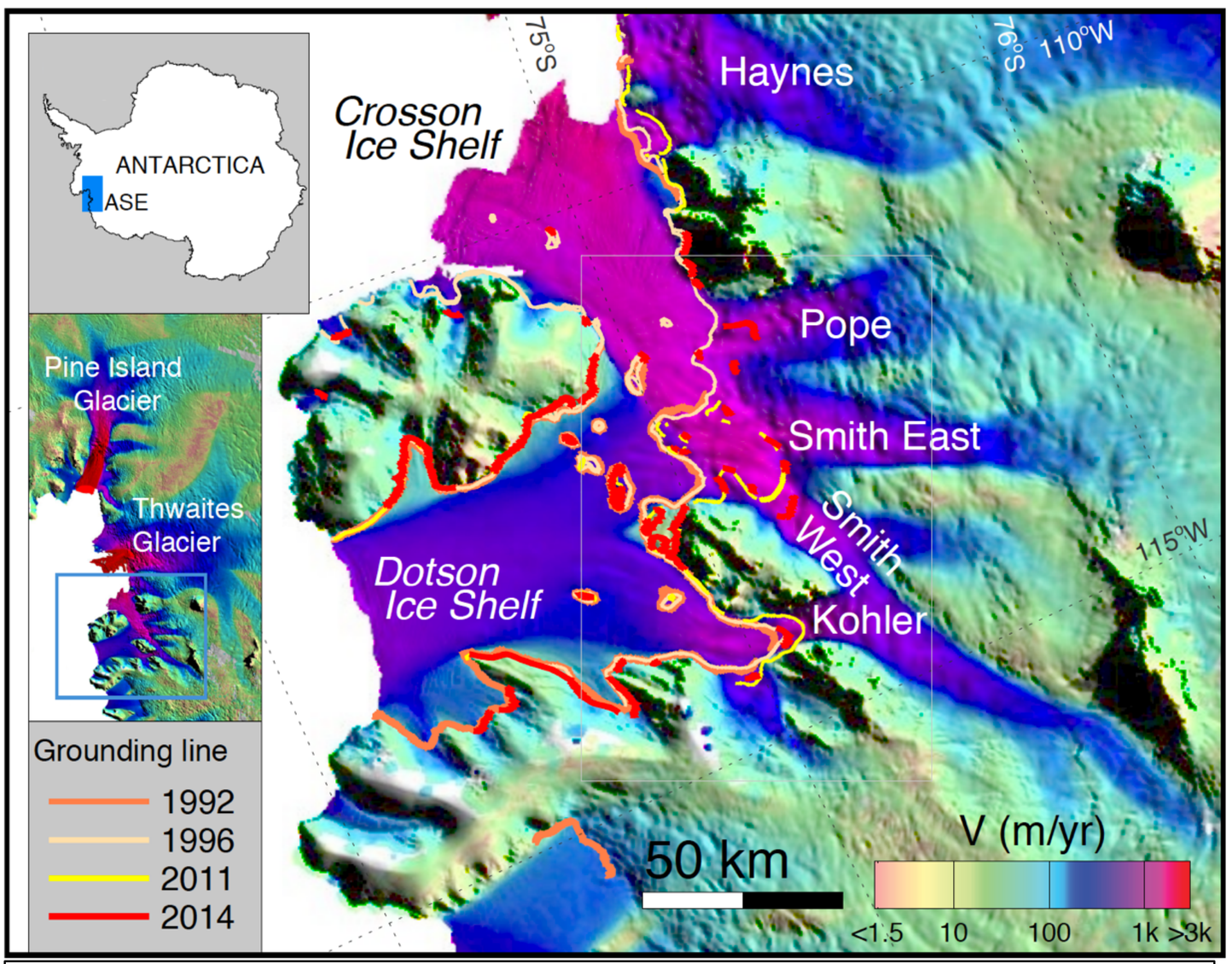

Ice velocity combining various data sets overlaid on a Moderate Resolution Imaging Spectro-radiometer (MODIS) mosaic of Antarctica. and currently available grounding lines for Pope, Smith, and Kohler Glaciers.
(From Scheuchl, B., J. Mouginot, E. Rignot, M. Morlighem, and A. Khazendar (2016), Grounding line retreat of Pope, Smith, and Kohler Glaciers, West Antarctica, measured withSentinel-1a radar interferometry data, *Geophys. Res. Lett.*, *43*,doi:10.1002/2016GL069287.)

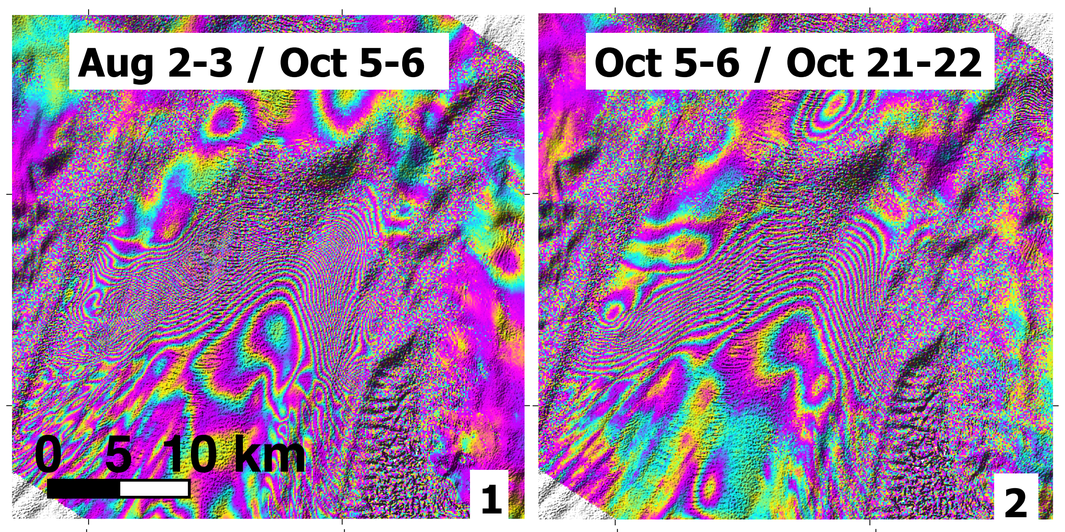

COSMO-SkyMed double difference SAR interferograms combining data from August to December 2015 over Pine Island Glacier. Given the large perpendicular baselines topography has been removed using a 5m TanDEM-X DEM. We observe a tidal induced migration for the grounding line of the order of 2 km.

Scientific Challenge

Understanding the potential instability of the Amundsen Sea Embayment (ASE) and the possible timescales of ASE disintegration are amongst the fundamental problems in modern glaciology. ASE is a marine-based ice sheet with a deepening inland bed, a configuration deemed to be unstable. ASE contains enough ice to raise global sea level more than 136 cm. While a number of studies have inferred the mechanical properties of portions of ASE using observationally constrained numerical models, these studies offer only temporal snapshots of basal mechanics owing to a dearth of observational time series.
Grounding zones migration on time scales characteristic of ocean tides and the importance of this migration in ice-stream-scale flow is an important unanswered questions that underlie uncertainties about the mechanics of ASE beds and inform our synthetic aperture radar (SAR) constellation-based observational strategy.

Strategic Importance

The Amundsen Sea Embayment (ASE) is undergoing significant changes and it is important to collect a data record of ice velocity and grounding line to provide boundary conditions for ice sheet modelers. Using 1-day CSK repeat pass data, we provide frequent, high-resolution grounding line measurements of Pine Island Glacier (PIG). The richness of the data set available allows us to show tide induced grounding line migration for this glacier for the first time.
The importance of this project can be summarized as follows:
- **Planning and executing the collection of a unique dataset using the only SAR mission available to date that can collect 1-day repeat pass data**
- **Provide frequent grounding line measurements at different tide levels**
- **Collect grounding line information in areas of fast flow, where CSK is the only mission available to collect suitable data**

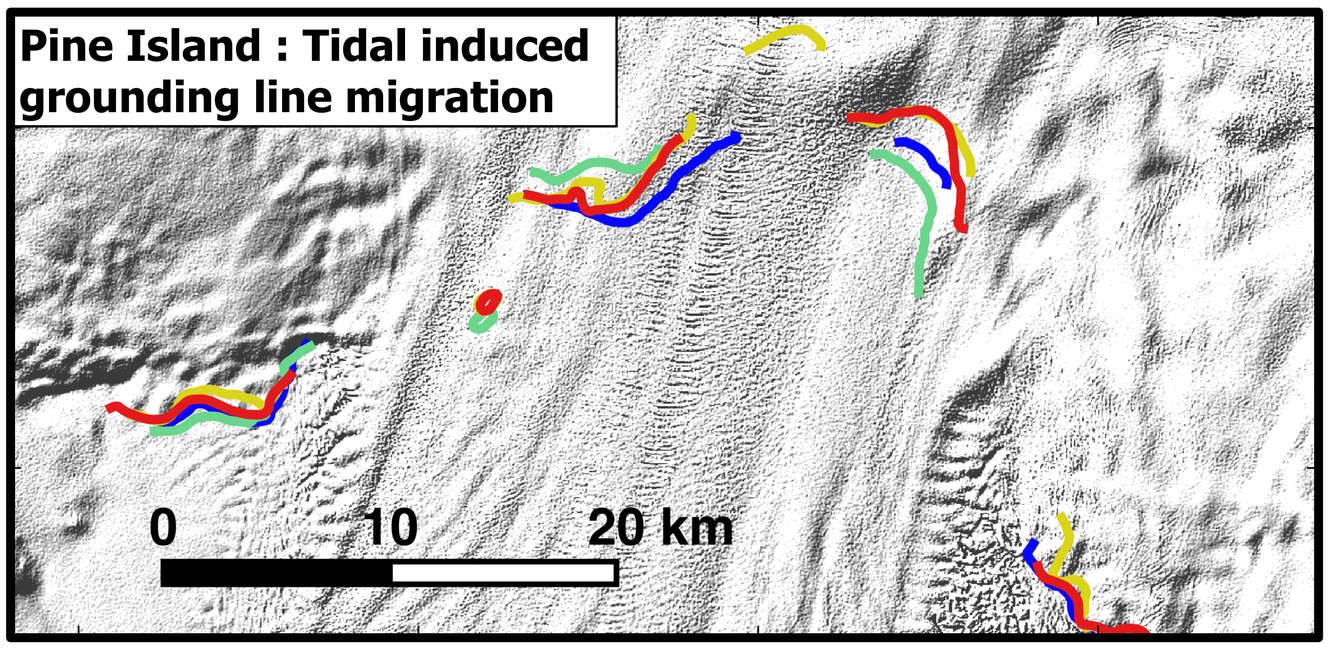

National Aeronautics and Space Administration
Jet Propulsion Laboratory
California Institute of Technology
Pasadena, California

www.nasa.gov

Poster No. EA-9

National Aeronautics and Space Administration

Amundsen Sea ocean, sea ice, and thermodynamic ice shelf simulation with optimized model parameters

Author: Yoshihiro Nakayama (329C)

Dimitris Menemenlis (329C), Michael Schodlok (329C), Eric Rignot (3340)

- Significantly better match with observations than previous modeling studies in this region, especially for Winter Waters (WW).
- Contrary to earlier work, this study suggests that local surface heat loss cannot fully explain the 2012 Pine Island Glacier (PIG) melt decrease.
- This study will lead to improved representation of ice-shelf ocean interactions in Estimating the Circulation and Climate of the Ocean (ECCO).

1. Why do we study Amundsen Sea (AS)?

- Warm CDW (Circumpolar Deep Water) → Ice shelf thinning → Speed up ice flow → Grounded ice loss → Sea level rise
- Increased melt in AS → Freshening locally and downstream → Thermohaline circulation weakening

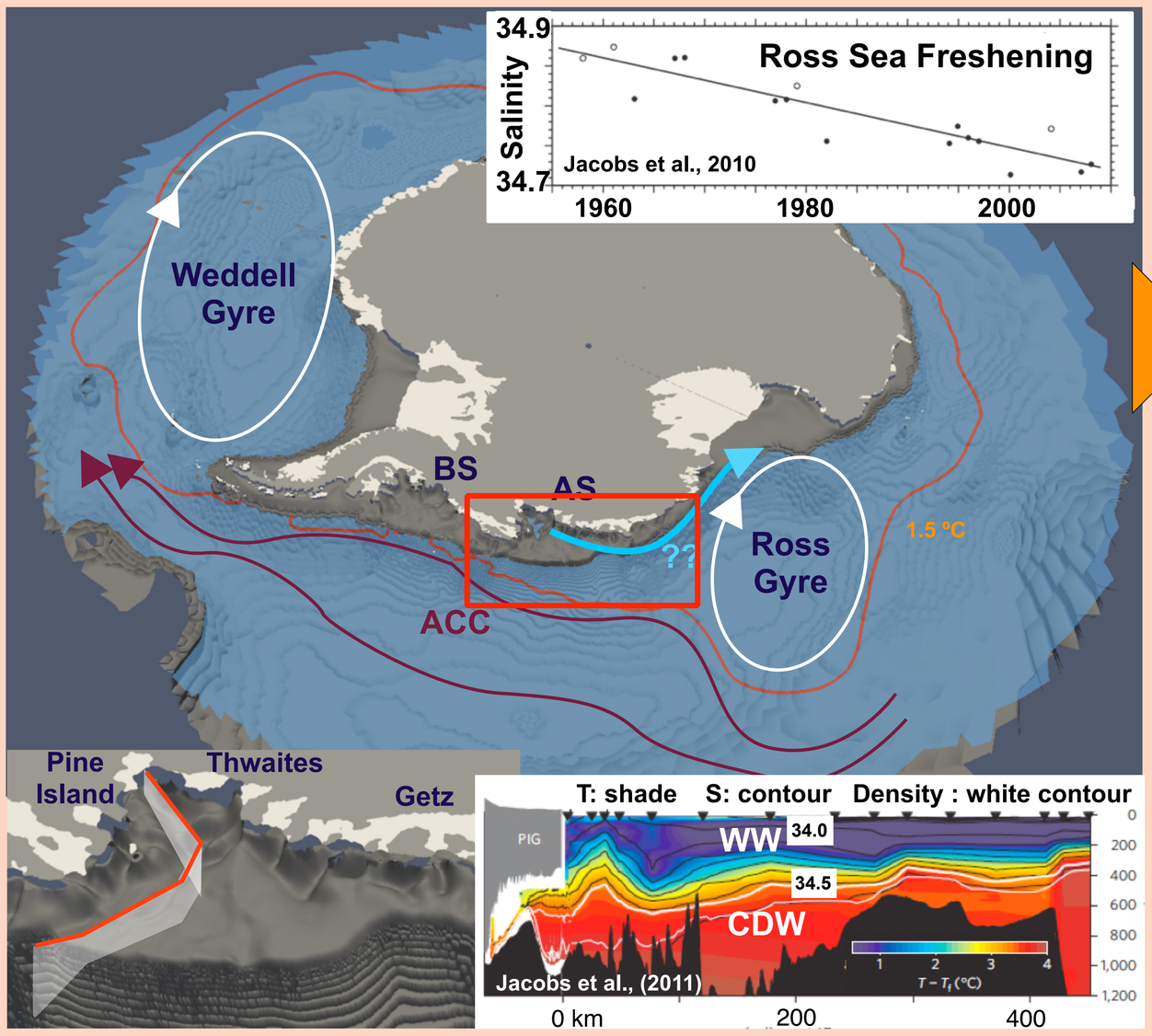

- We fit the model to the available oceanographic observations using property-conserving estimation approaches developed by ECCO.
- This study
  - (1) increases understanding of mechanisms controlling ice loss,
  - (2) provides optimized AS simulation for sea level rise projections, and
  - (3) develops improved representation of ocean-ice shelf interactions at a resolution consistent with current-generation ocean retrospective analyses and global climate models.

2. MITgcm regional AS configuration

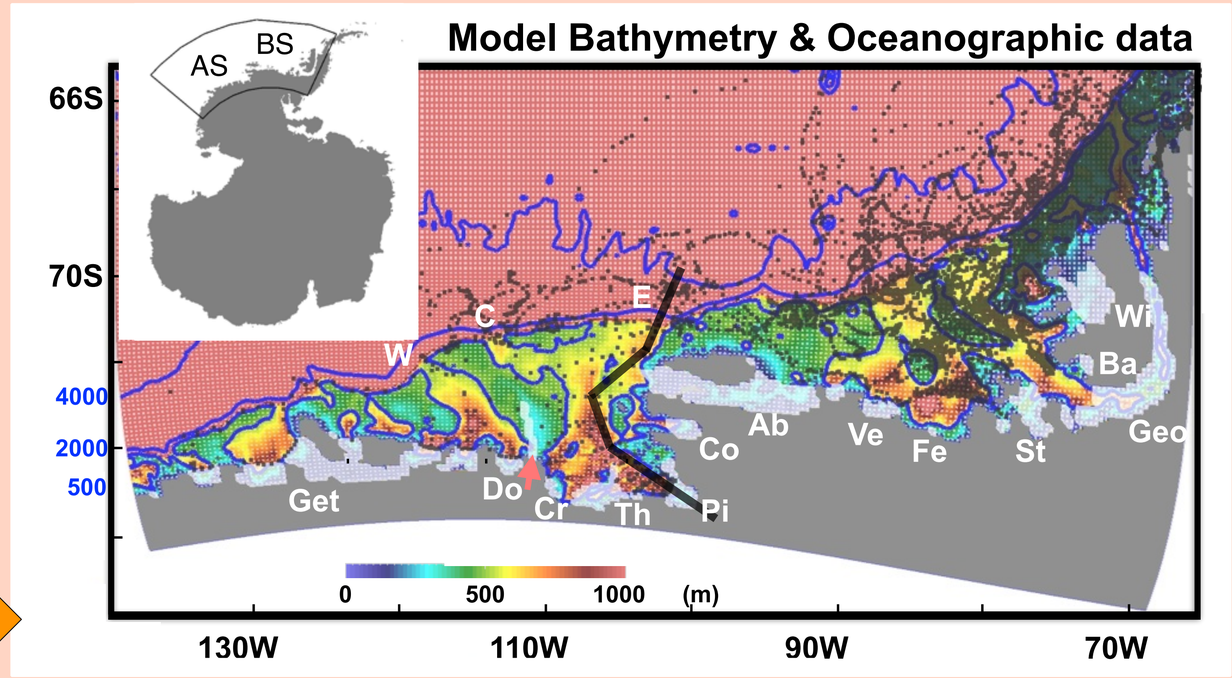

- Horizontal grid spacing of ~10 km and 50 vertical levels.
- Bathymetry from IBSCO and ice shelf draft from BEDMAP.
- Initial condition from WOA 2013 and boundary conditions from ECCO.
- 10-year simulation (2001-2010) with ECCO atmospheric forcing.

3. Model simulation agrees well with observations.

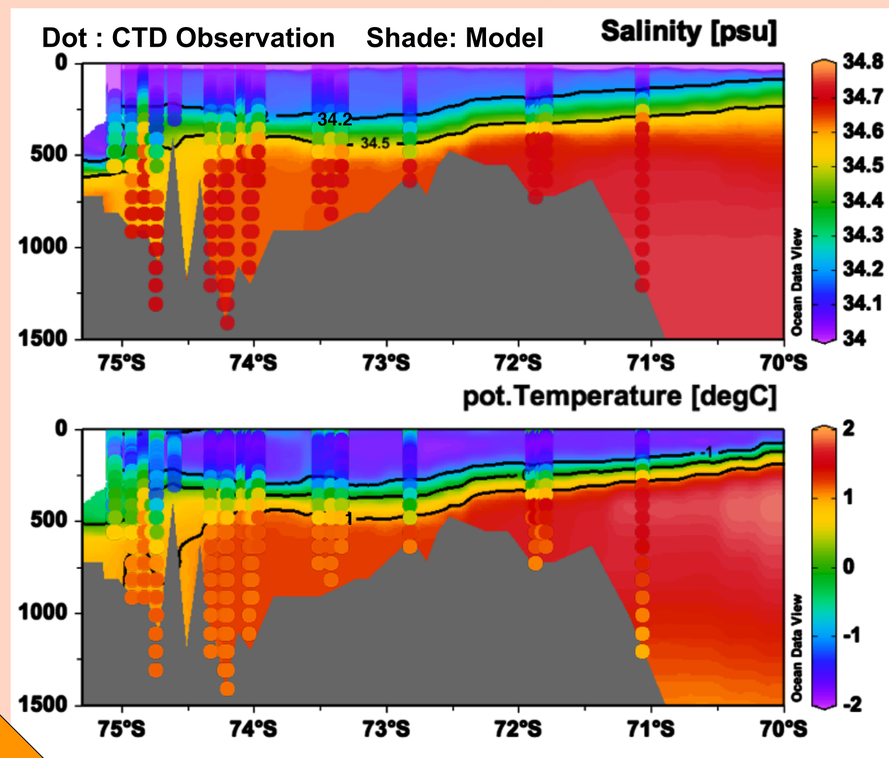

WW has similar properties and thickness (~250m).

CDW has similar properties and thickness.

Best match to observations compared to all other modeling studies.

4. Why PIG melt decreases in 2012?

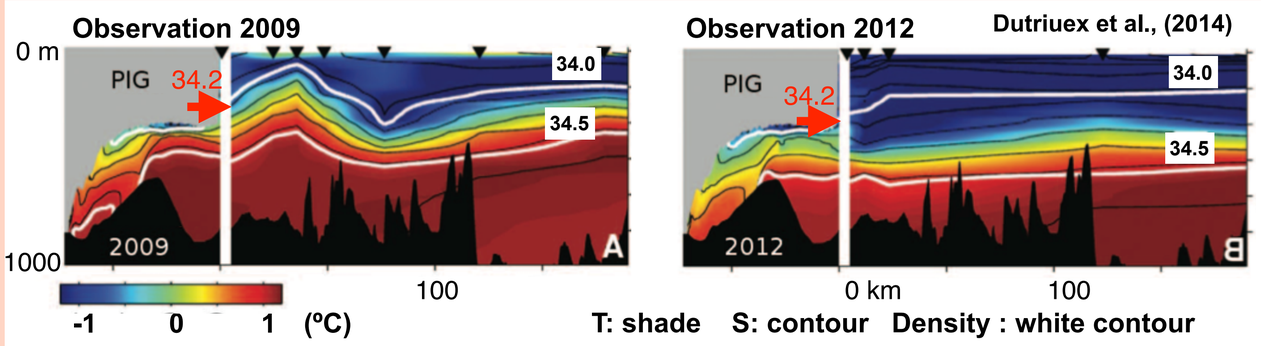

Observations show WW thickening, cooling, and freshening from 2009 to 2012.

Is this caused by an increase in local surface heat loss as suggested by previous study ?

Model sensitivity experiments (120% surface heat flux)

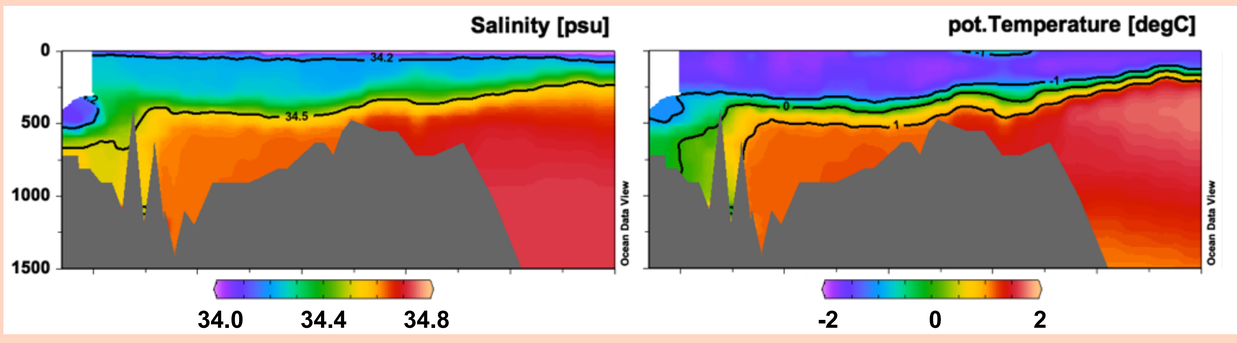

Model sensitivity experiments show WW thickening, cooling, but not freshening, indicating that local surface heat loss cannot fully explain the 2012 PIG melt decrease.

Poster No. EA-10

National Aeronautics and Space Administration

Sensitivity of west Antarctic Peninsula glaciers to ocean warming in the decades after Wordie Ice Shelf collapse

Author: Catherine C. Walker (329C), Alex S. Gardner (329C)

1. Evidence of rapid dynamic thinning from Wordie Ice Shelf

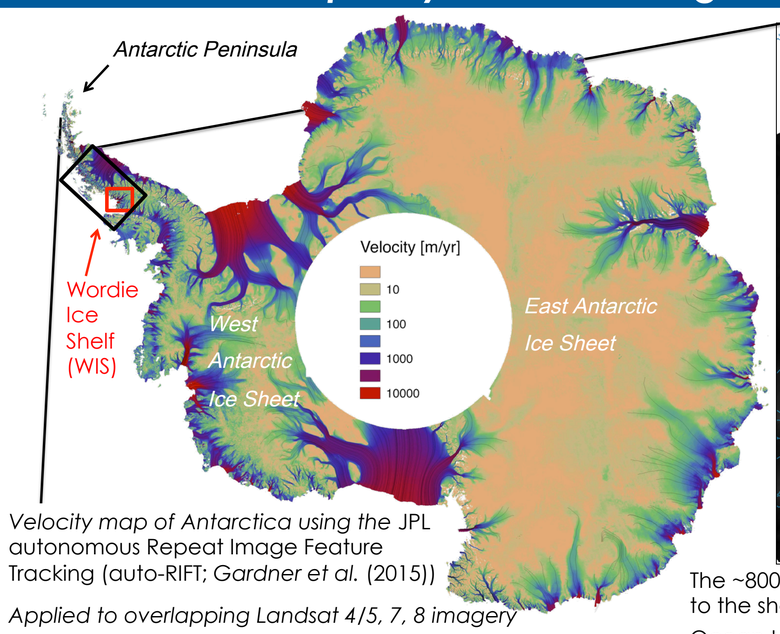

Velocity map of Antarctica using the JPL autonomous Repeat Image Feature Tracking (auto-RIFT; *Gardner et al.* (2015))

Applied to overlapping Landsat 4/5, 7, 8 imagery

The **WIS** is located on the west Antarctic Peninsula (**WAP**) in Marguerite Bay (~25,000 km^2)

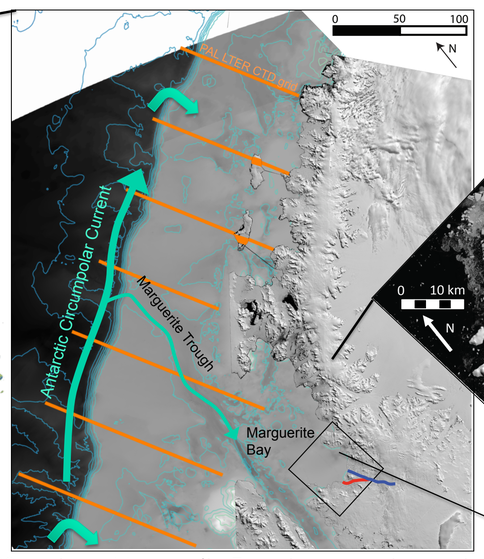

The ~800 m-deep Marguerite Trough connects coastal areas to the shelf break

Ocean temperature and salinity are changing on the continental shelf, associated with warming and shoaling of deep water off-shore (e.g., *Schmidtko et al.*, 2014)

The Antarctic Circumpolar Current (ACC) lies just offshore of the west Antarctic Peninsula (WAP), and warm, salty Circumpolar Deep Water (CDW) close to the shelf break, where it can access the continental shelf via troughs (e.g., Marguerite Trough)

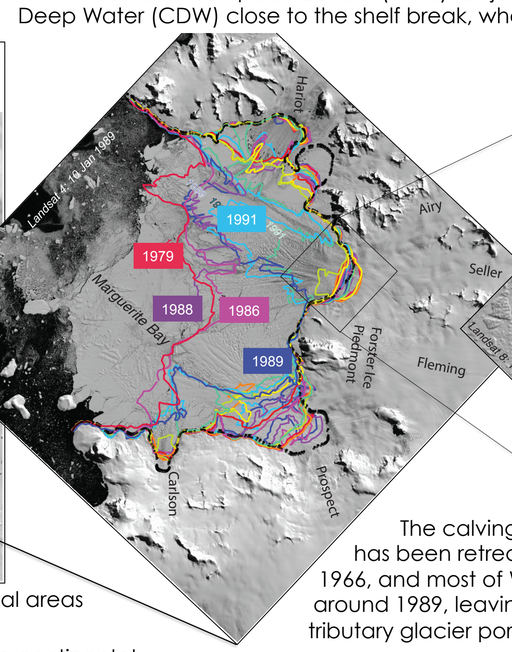

The calving front has been retreating since 1966, and most of WIS collapsed around 1989, leaving only floating tributary glacier portions remaining

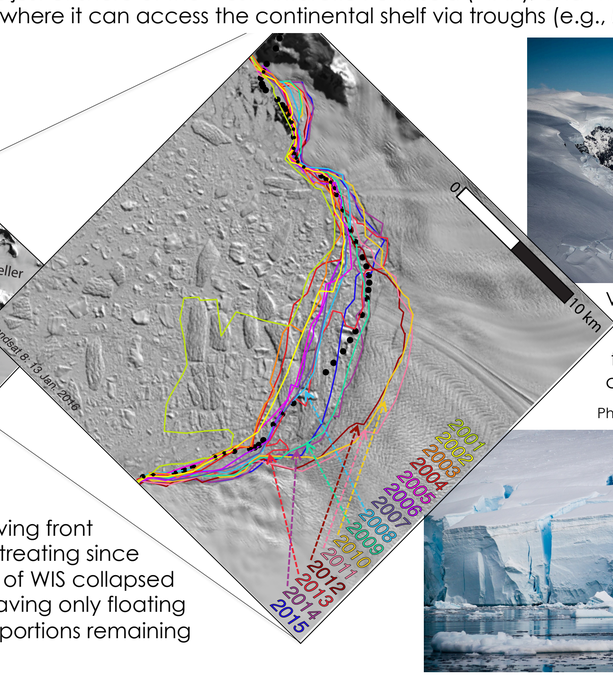

Views of Fleming Glacier from a NASA IceBridge flight in 2014 (top) and its calving front (below)

Photo Credits: M. Studinger, M. Braun

Velocity change over time (dv/dt):

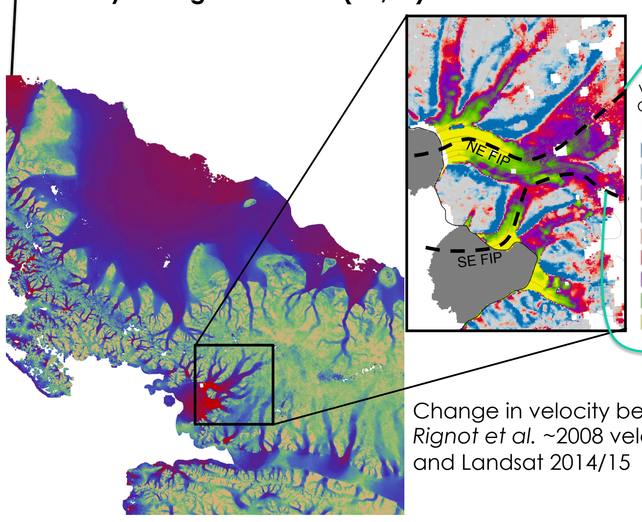

Change in velocity between *Rignot et al.* ~2008 velocities and Landsat 2014/15

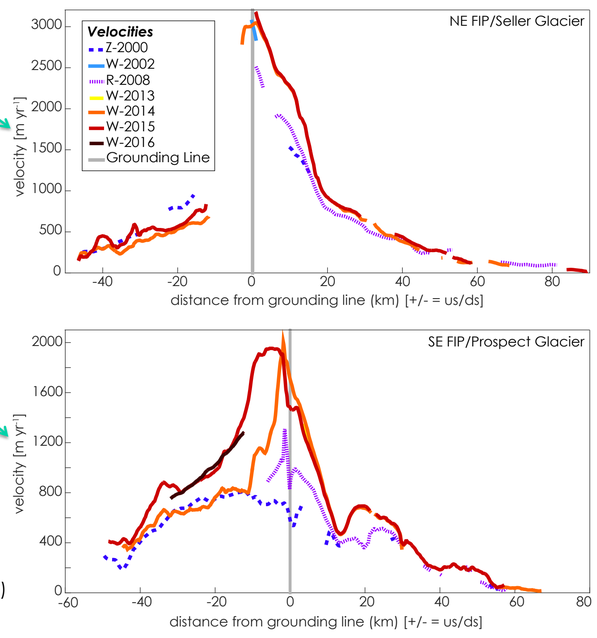

Total flux into MB: 20.5 Gt/yr (using Huss and Farinotti (2014) bed topography)
Change in flux 2008-2014: 5.6 Gt/yr

Elevation change over time (dh/dt):

- Airborne Topographic Mapper (ATM) laser altimetry from NASA's Operation IceBridge (OIB, 2002-present)
- L2 data product (50 m spacing) corrected for changing glacier slope at each point

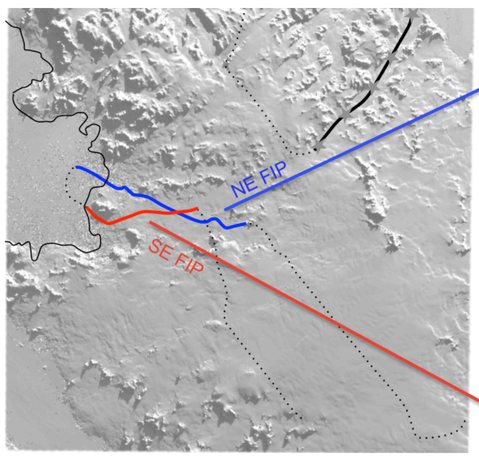

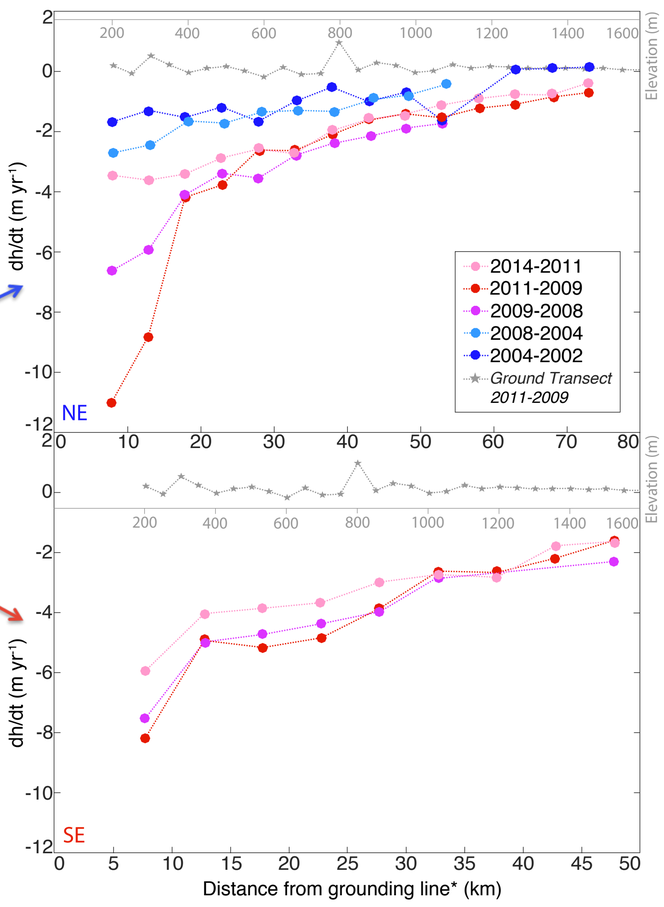

Basal topography of WIS tributaries:

- Multi-channel Coherent Radar Depth Sounder (MCoRDS) from NASA's OIB showed they are grounded at approx. 600 to 800 m below sea level

2. What caused the rapid drawdown?

Seal-borne hydrography observations:

Marine Mammals Exploring the Oceans Pole-to-pole (MEOP) CTD program: ~300,000 profiles since 2004

Left: Maximum temperatures of profiles taken from 2006-2010 at 300 m depth (MB average ~1.7°C)

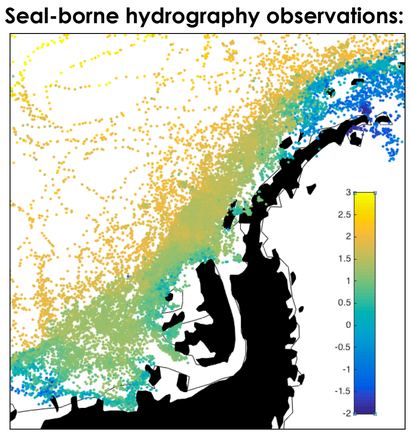

Right: Temperature-salinity plot shows the changing water properties over time (2006-2009) in Marguerite Bay. Note water in 2009 was warmer than water masses in other years.

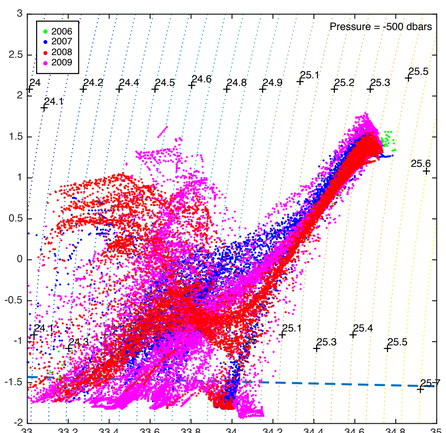

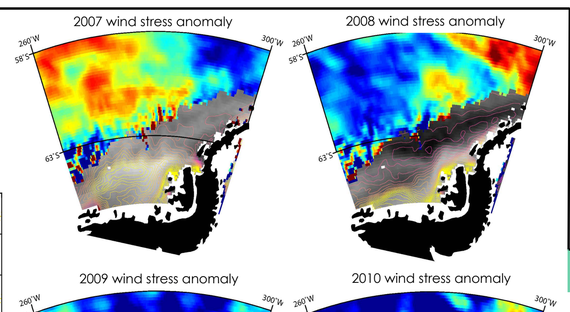

Above: Wind stress curl anomalies from JPL-ECCO2. Negative curl implies upwelling of warm, salty CDW; positive values imply downwelling. Sea ice extent shown in gray. Increased upwelling is observed in 2009-2010.

Where did the warm water come from?

Below: Sea ice concentration in (top) Marguerite Bay (MB, red) and eastern Bellingshausen Sea (BS, blue). Middle: Blue and yellow lines - Winter in BS and MB; Orange and purple lines - spring in BS and MB. *Note: anomalously low sea ice concentration in winter and spring 2008*
Bottom: net surface heat flux (Qnet) of the Bellingshausen Sea basin, essentially showing heat content of the water offshore

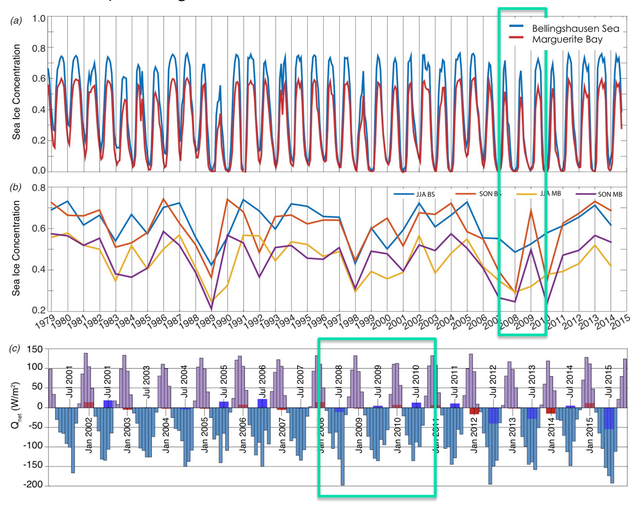

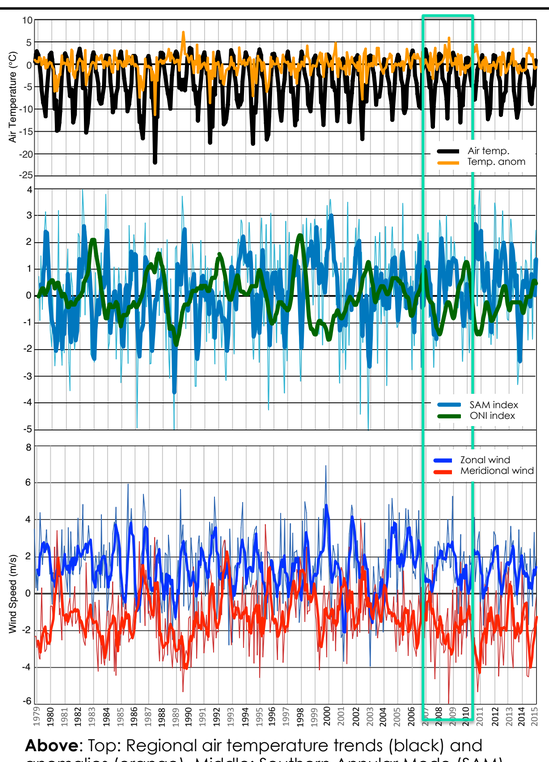

Above: Top: Regional air temperature trends (black) and anomalies (orange). Middle: Southern Annular Mode (SAM) index in blue and El Nino-Southern Oscillation (ENSO/ONI) index in green. Bottom: Zonal (u) in blue and meridional (v) wind in red in the Bellingshausen Sea region, NCEP Re-analysis data, 1979-2015

PAL LTER CTD measurements of oceanic changes:

Below: L200 – Shelf break to coast along-grid profile over Bedmap2 bathymetry (**A – B**)

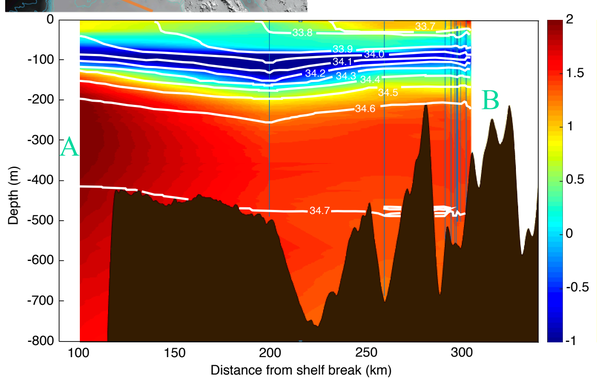

Site A: CTD sampling of hydrography at shelf break/entrance to Marguerite Trough
Site B: CTD-measured hydrography at the sampling location closest to Wordie Ice Shelf

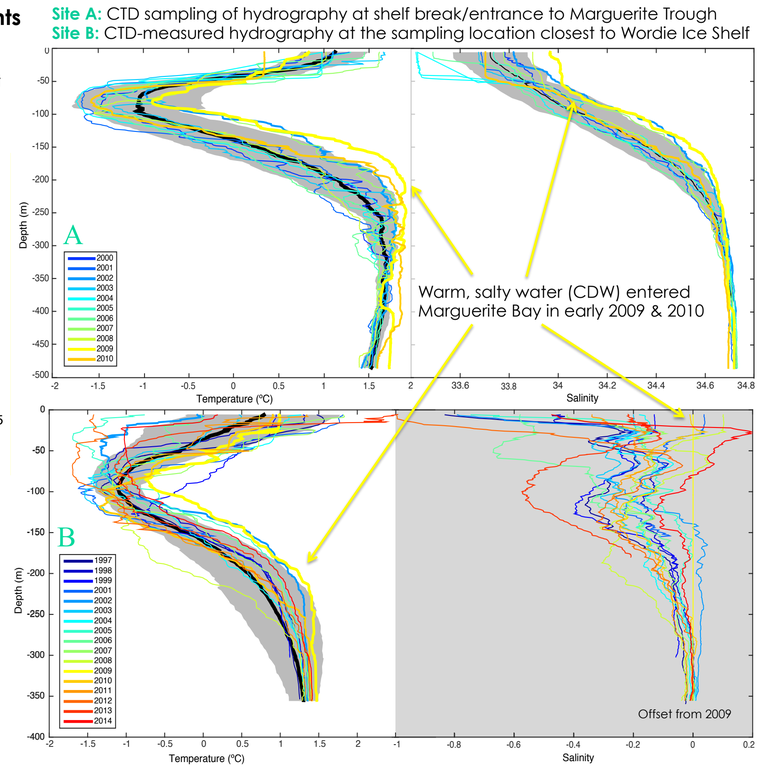

Summary | Conclusions:

- WIS tributaries accelerated ~500 m/yr between 2008 InSAR- and 2014/2015 Landsat-derived velocities
- dh/dt from IceBridge laser altimetry (ATM) showed rapid drawdown between 2008 and 2014 (most between 2009-2011)
- Basal topography from the Multi-channel Coherent Radar Depth Sounder (MCoRDS) from NASA's OIB
- Ocean water in MB in 2009 had shallowest thermocline since 1993.
  - *Anomalously high ocean heat content on WAP 2008-2010*
- Ekman pumping/upwelling (increasingly negative wind stress curl) dominated in BS between 2008-2010
- Winter and summer Q_{net} (ocean-air heat flux) was anomalously high in east BS from July 2009 – July 2011
- ***Mid-depth heat content and upwelling tied to regional trends?***
  - *Low pressure systems off WAP and delivery of CDW is consistent with changes in the state of ENSO (La Nina drives enhanced upwelling in this region) and in the strength of the Southern Annular Mode: +SAM drives a local response similar to that of La Nina (e.g., Martinson et al., 2008),*
  - *+SAM occurred with La Nina concurrently from late 2007-end of 2008, and 2010!*

Poster No. EA-11

National Aeronautics and Space Administration

Jet Propulsion Laboratory
California Institute of Technology
Pasadena, California

www.nasa.gov

National Aeronautics and Space Administration

Climate and Polar Motion During the GRACE Period

Surendra Adhikari (329C-Affiliate)
Erik R. Ivins (329C) and Eric Larour (329C)

Context

Polar Motion: Polar motion is the movement of Earth's spin axis as it wanders through the crust. It can be understood as a 2D position vector, with x and y components pointing along the longitudes of 0° and 90° east, respectively.

Observations: The 115-year polar motion record suggests the following (Fig. 1).

- ✓ Since about 2000, the linear drift direction has deviated substantially from its long-term direction that is related to glacial isostatic adjustment (GIA).
- ✓ Interannual variability persists, in spite of the new drift direction.

Research Objectives: To identify the physical mechanisms that explain these enigmatic features of polar motion during the GRACE period (2003–2015).

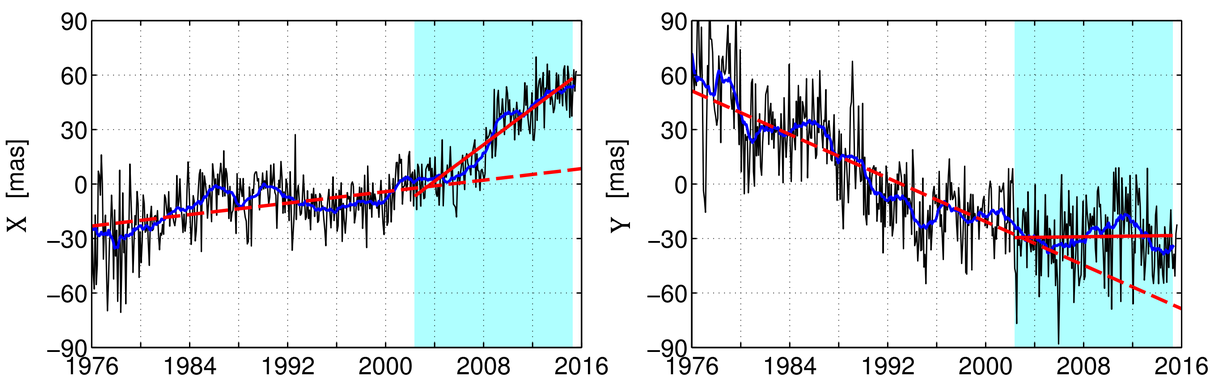

Fig. 1: Observed pole position. x and y components of (mean monthly) pole position vector (black) obtained after filtering 433-day Chandler and shorter timescale wobbles. Smoothed solutions (blue) reveal interannual variability about the 20th century linear trend (dashed red). Cyan shadows in the background cover the GRACE period, over which the drift direction deviates (solid red) from the 20th century trend. **[Note: 1 mas ≈ 3.09 cm]**

Data and Methods

Theory: Climate-driven mass transport on Earth's surface perturbs the inertia tensor $\boldsymbol{I}(t)$. Corresponding change in angular velocity $\boldsymbol{\omega}(t)$, which characterizes the polar motion, is obtained by solving the following Euler's equation.

$$\frac{\mathrm{d}}{\mathrm{d}t}[\boldsymbol{\omega}(t)\cdot\boldsymbol{I}(t)] + \boldsymbol{\omega}(t)\times[\boldsymbol{\omega}(t)\cdot\boldsymbol{I}(t)] = \mathbf{0}$$

Mass transport: We use GRACE (CSR R-05 L-2) observations of continental mass change and compute the corresponding ocean mass redistribution by solving the self-attraction & loading problem on an elastic, rotating earth (Fig. 2).

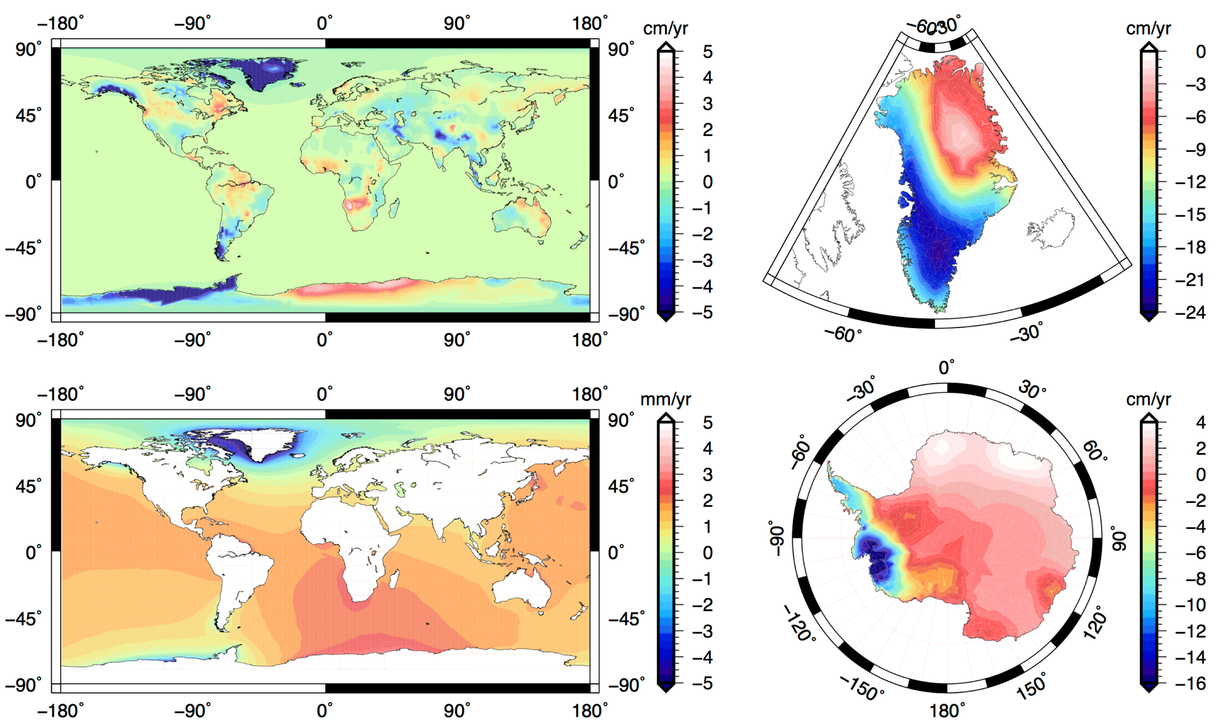

Fig. 2: Climate-driven mass transport. **(a)** Rate of mass change (water-height per year) on Earth's surface. Solutions are reproduced for **(b)** Greenland, **(c)** Antarctica, **(d)** the oceans.

Results and Implications

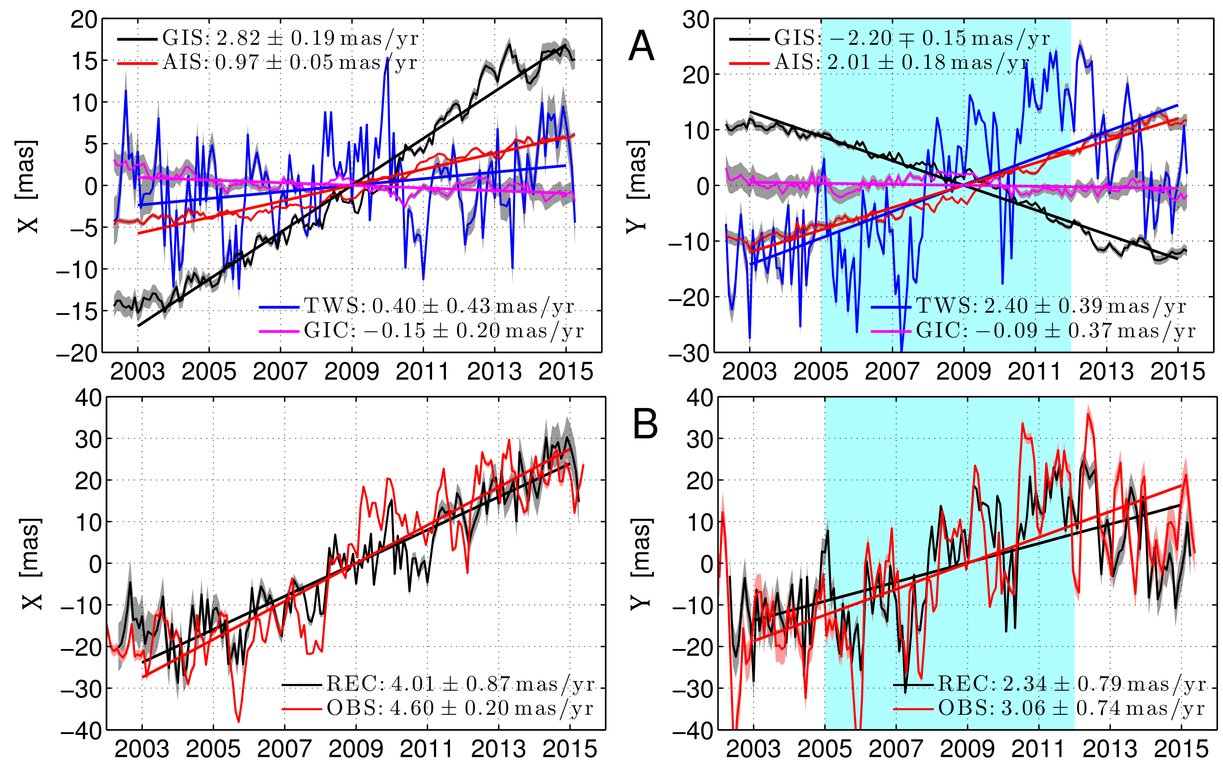

Fig. 3: Climate-driven polar motion. **(a)** Polar motion excitations caused by four sources: Greenland (GIS), Antarctica (AIS), global glaciers and ice caps (GICs), and terrestrial water storage (TWS). **(b)** Total reconstructed (REC) and observed (OBS) excitations. We remove the 20th century linear trends from OBS. Notice that reversal in y motion is related to TWS.

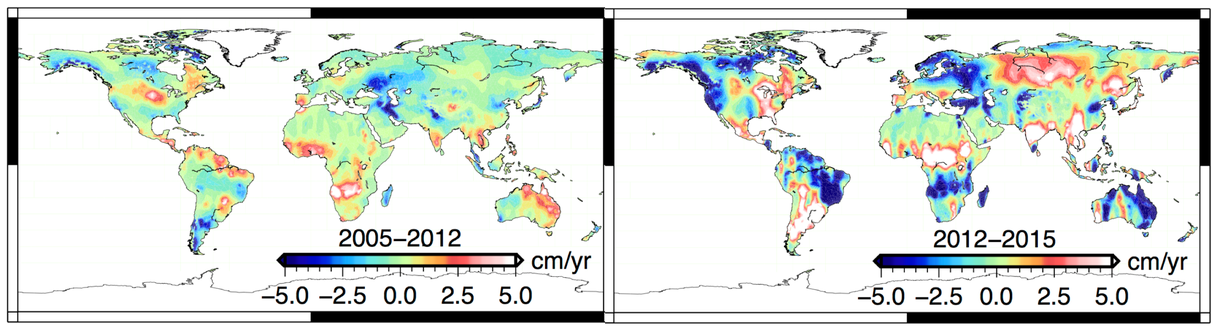

Fig. 4: Spatiotemporal variability in TWS. Reversal in global 'wet-dry' pattern (after 2012) is responsible for the observed interannual variability in y motion (see Figs. 1 and 3).

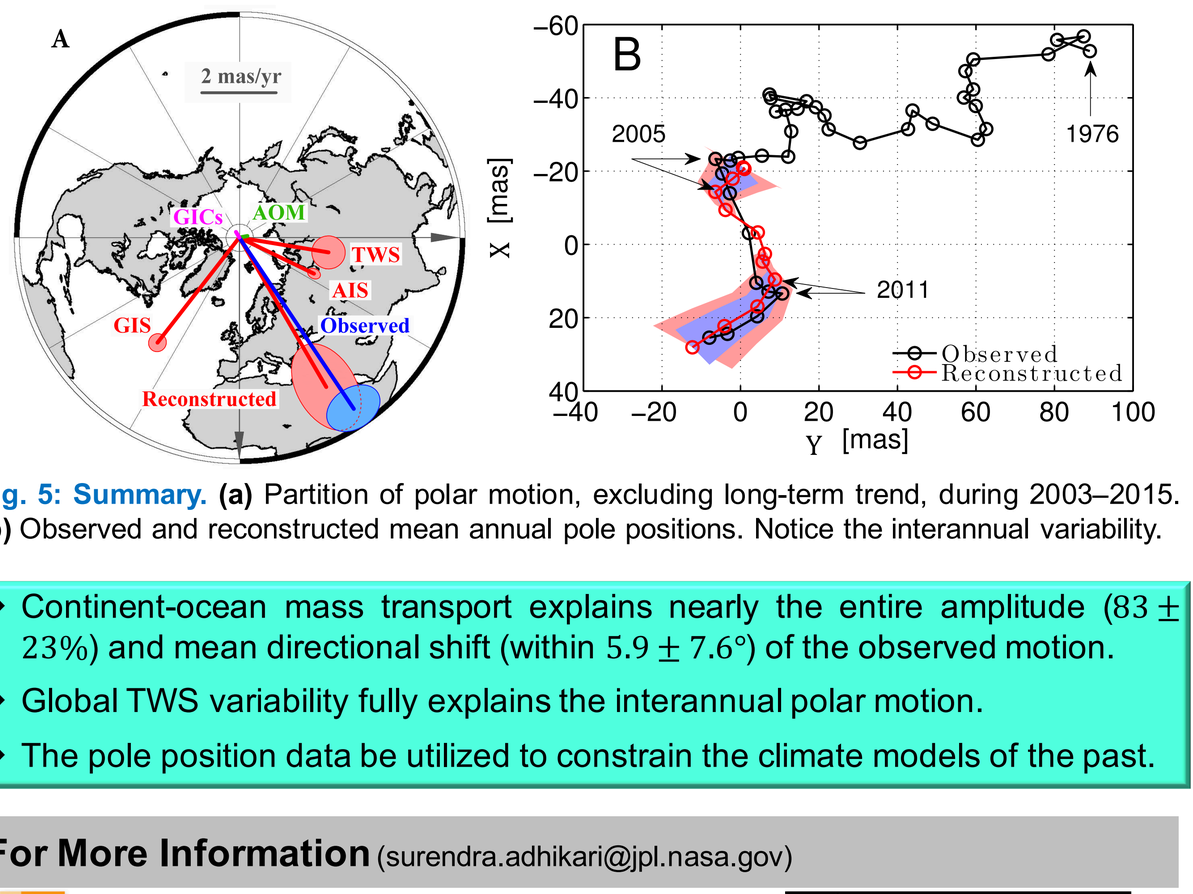

Fig. 5: Summary. **(a)** Partition of polar motion, excluding long-term trend, during 2003–2015. **(b)** Observed and reconstructed mean annual pole positions. Notice the interannual variability.

- ❖ Continent-ocean mass transport explains nearly the entire amplitude ($83 \pm 23\%$) and mean directional shift (within $5.9 \pm 7.6°$) of the observed motion.
- ❖ Global TWS variability fully explains the interannual polar motion.
- ❖ The pole position data be utilized to constrain the climate models of the past.

For More Information (surendra.adhikari@jpl.nasa.gov)

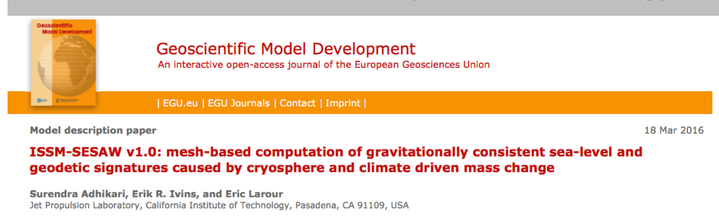
Geoscientific Model Development
An interactive open-access journal of the European Geosciences Union
| EGU.eu | EGU Journals | Contact | Imprint |
Model description paper 18 Mar 2016
ISSM-SESAW v1.0: mesh-based computation of gravitationally consistent sea-level and geodetic signatures caused by cryosphere and climate driven mass change
Surendra Adhikari, Erik R. Ivins, and Eric Larour
Jet Propulsion Laboratory, California Institute of Technology, Pasadena, CA 91109, USA


Science Advances AAAS
RESEARCH ARTICLE | CLIMATOLOGY
Climate-driven polar motion: 2003–2015
Surendra Adhikari* and Erik R. Ivins
+ Author Affiliations
*Corresponding author. E-mail: surendra.adhikari@jpl.nasa.gov
Science Advances 08 Apr 2016:
Vol. 2, no. 4, e1501693
DOI: 10.1126/sciadv.1501693

National Aeronautics and Space Administration
Jet Propulsion Laboratory
California Institute of Technology
Pasadena, California

www.nasa.gov

This research was carried out at the **Jet Propulsion Laboratory** and the **California Institute of Technology** under a contract with the **National Aeronautics and Space Administration** and funded through the **NASA Postdoctoral Program** fellowship.

Poster No. EA-13

National Aeronautics and Space Administration

The first centimeter-scale 3D model of a volcanic conduit

Principal Investigator: Carolyn Parcheta (3223)

Jeremy Nash (347H), Aaron Parness (347C), Karl Mitchell (3223)

Fig. 3a

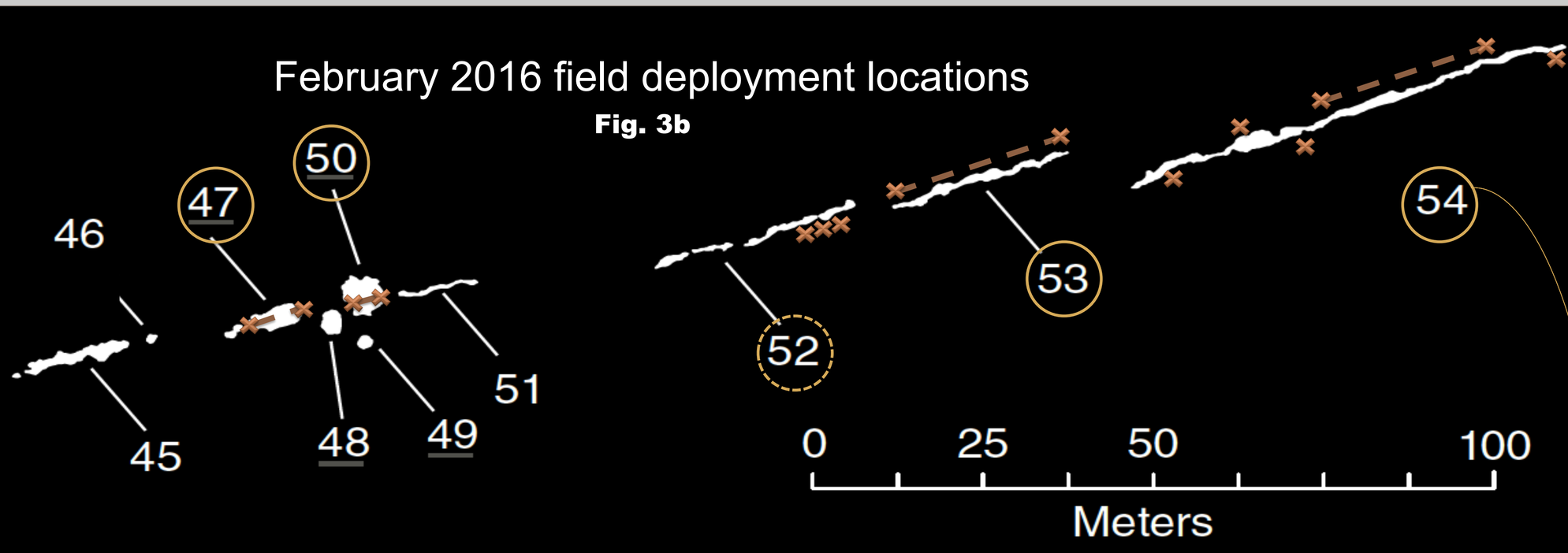

Introduction

Fig. 1

Basaltic fissure eruptions (Fig 1) are the most common eruption style and mechanism in the solar system. Obtaining data of volcanic fissure conduits has previously been impossible because fissures are:

- too thin for geophysical methods, or
- buried by eruption deposits

To understand and extrapolate eruption behavior, hazards, and planetary evolution, researchers and modelers have traditionally assumed a first-order (planar) feature to represent fissures.

Problem

*On magmatic (not tectonic) scales, fissure conduits may **NOT** be vertical or parallel-walled*

Methodology

We have developed VolcanoBot (Fig 2) to acquire the first robust and diagnostic data of eruptive fissure conduit geometries. *This is the only platform in the world that can currently collect such data, due to it's size, vertical mobility, and ruggedized components.*

The engineering and computer vision developments were presented at Postdoc Day 2014 and 2015. VolcanoBot uses near infra-red structured light during field deployment (Fig 3) to create surface mesh 3d models of the conduit geometries (Fig 4).

Fig. 2

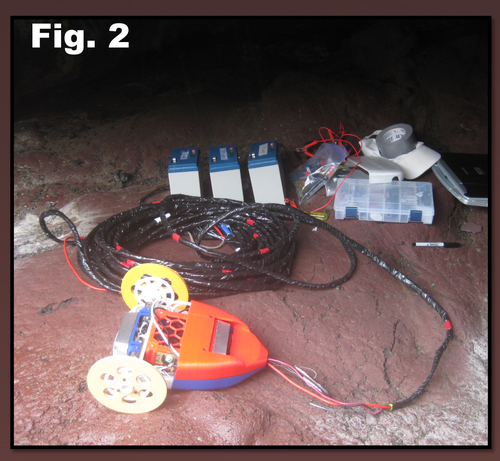

Selected 3D Model Results

Fig. 4

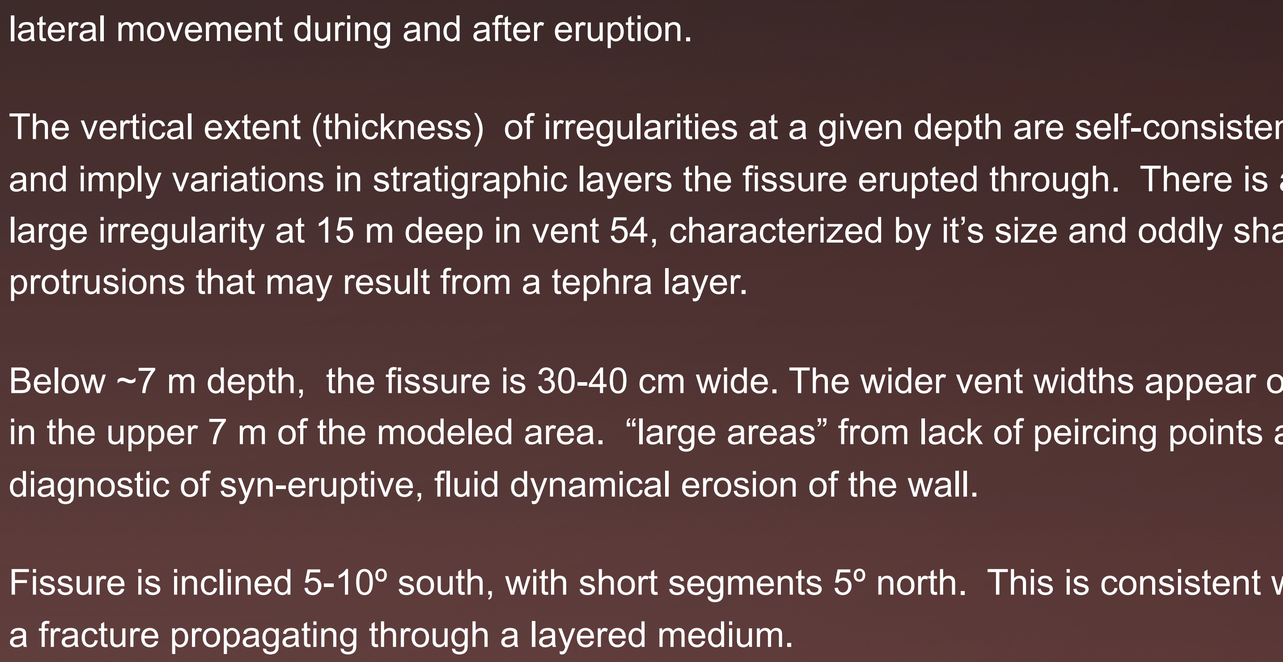

Interpretations

Shallow subsurface irregularities protrude 30-50 cm into the fissure and are 1-2 m long. They are matched by similar sized cavities on the opposing wall, indicating little lateral movement during and after eruption.

The vertical extent (thickness) of irregularities at a given depth are self-consistent, and imply variations in stratigraphic layers the fissure erupted through. There is a large irregularity at 15 m deep in vent 54, characterized by it's size and oddly shaped protrusions that may result from a tephra layer.

Below ~7 m depth, the fissure is 30-40 cm wide. The wider vent widths appear only in the upper 7 m of the modeled area. "large areas" from lack of peircing points are diagnostic of syn-eruptive, fluid dynamical erosion of the wall.

Fissure is inclined 5-10º south, with short segments 5º north. This is consistent with a fracture propagating through a layered medium.

Acknowledgements

This work is funded by a *NASA Postdoctoral Fellowship* through **Universities Space Research Association** and took place at:

National Aeronautics and Space Administration
Jet Propulsion Laboratory
California Institute of Technology
Pasadena, California
www.nasa.gov

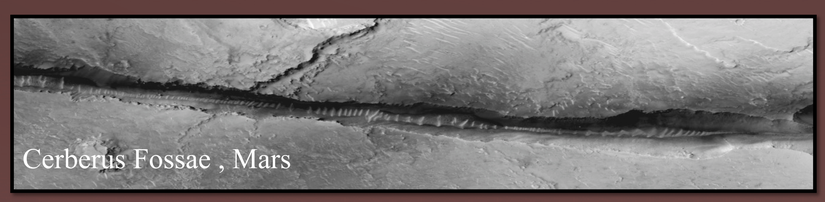

Importance

By correlating the subsurface conduit geometry with the surface expression of terrestrial eruptive fissures, we will be better able to understand fissures and cracks in rock and on Mars, Enceladus, and Europa during future missions.

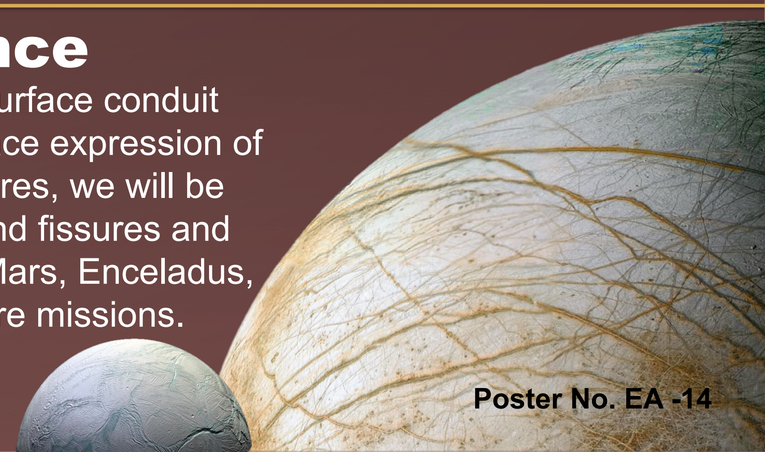

Poster No. EA -14

National Aeronautics and Space Administration

A Texas Flood From Land To Ocean Observed By SMAP

Séverine Fournier (329B), John Reager (329F), Tong Lee (329B), Jorge Vazquez (329B), Cédric David (329F) and Michelle Gierach (329G)
Jet Propulsion Laboratory, California Institute of Technology, Pasadena, California, USA, email : severine.fournier@jpl.nasa.gov

THE NEED TO MAP FLOOD IMPACTS ACROSS THE COASTAL INTERFACE

- Floods are among the most significant types of natural hazards affecting human society, terrestrial environment & marine ecosystems (changes in salinity & nutrients; input of terrigeneous toxic matter).
- A predictive system for severe ocean events would be beneficial.
- May 2015: record rainfall hit parched South Texas, causing a severe flooding.
- The **NASA's Soil Moisture Active Passive (SMAP) soil moisture and sea surface salinity (SSS)** now provide unique, complementary observations to map the lifecycle of flood events bridging the terrestrial and ocean domains.

SMAP SSS VALIDATION IN THE GULF OF MEXICO (GoM)

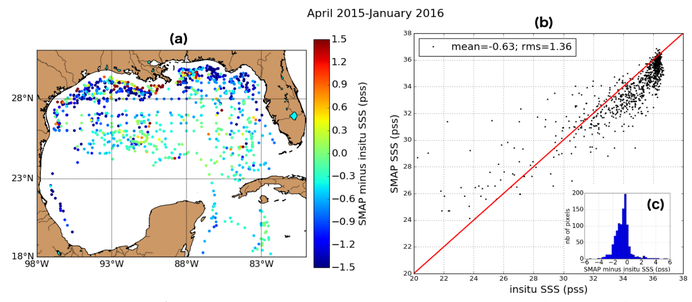

Fig 1: 8-day 0.25° SMAP SSS vs. co-located in situ SSS for 04/2015-01/2016 in the Gulf of Mexico (GoM): (a) time-mean difference, (b) scatterplot & histogram.

- SMAP : better resolution than Aquarius and less affected by Radio Frequency Interferences than SMOS
- SMAP SSS compare better with in situ SSS than SMOS SSS in the GoM, especially at lower salinity (SMOS versus in situ : rms 1.48 pss)
- Satellite/in situ SSS differences also affected by spatial & temporal scale mismatch and near-surface stratification (especially in regions with strong SSS horizontal & vertical gradients)

PROGRESSION OF THE 2015 TEXAS FLOOD ON LAND AND ITS IMPACT ON THE GoM

Fig 2: Monthly maps of precipitation, soil moisture, liquid water equivalent thickness, SSS, a_{cdm} and currents.

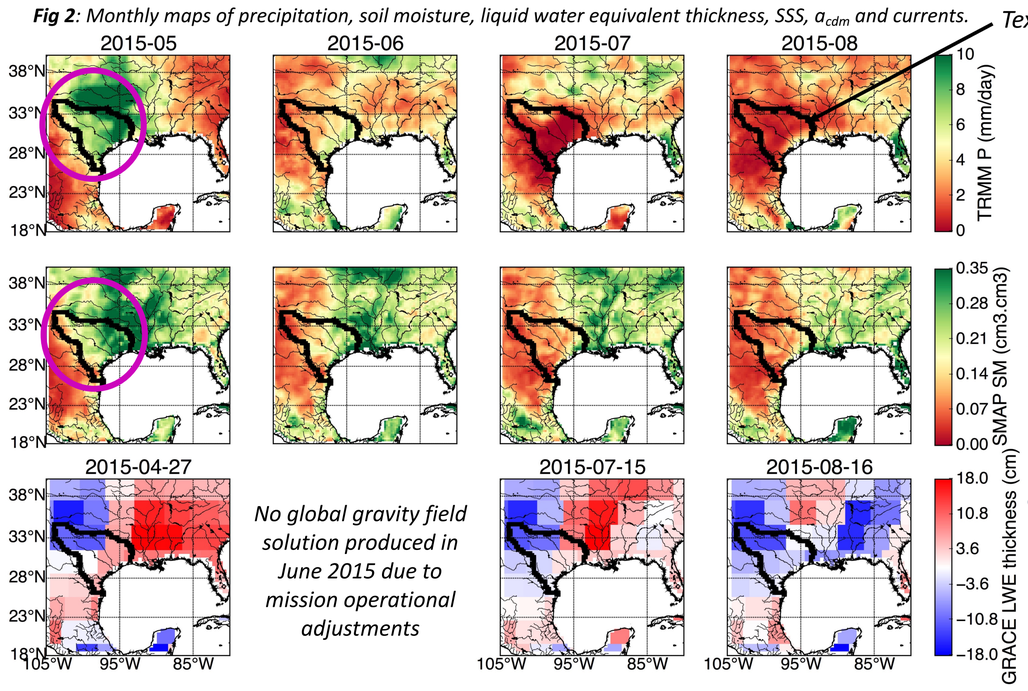

May 2015: Precipitation anomaly over Texas (over 2 trillion gallons), the strongest during the entire record of the study (7.5 mm/day)

May 2015: Saturation of surface soil moisture detected by SMAP, the strongest during the entire record of the study (0.23-0.29 units), consistent with precipitation

April-July 2015: No record-length maximum seen in terrestrial water storage after the flood but a local maximum relative to the ongoing drought

May 2015: Record-length peak over 6 years (2.5 times higher than in 2012, 21 times higher than in 2011). Most intense discharge in the northeastern portion of Texas

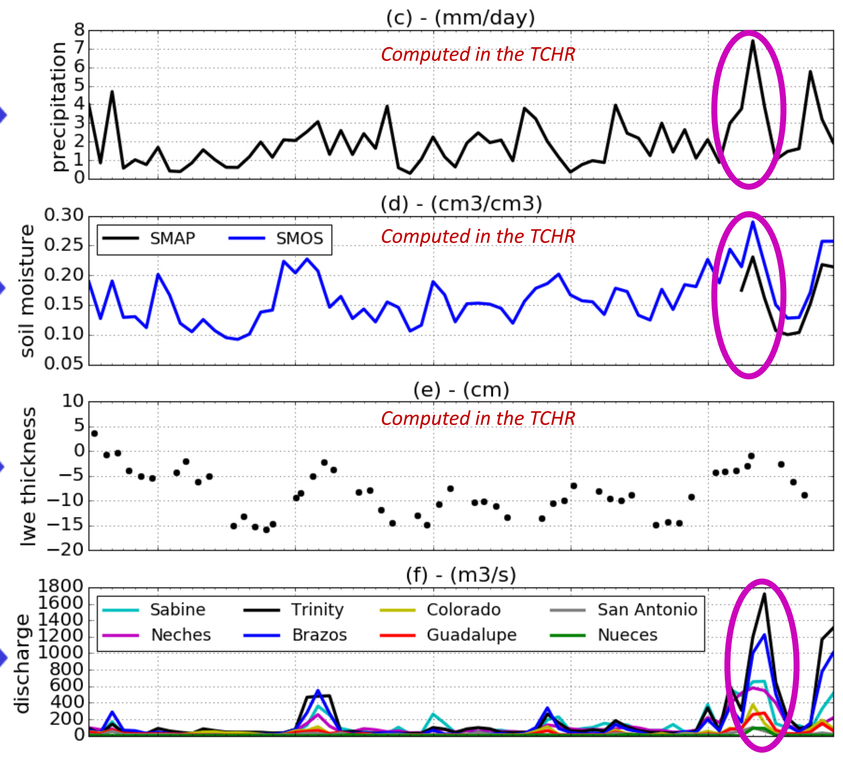

May: unusual freshwater plume emerges along the Texas coast

June: freshwater plume carried eastward

July-August: plume carried southward away from the shore

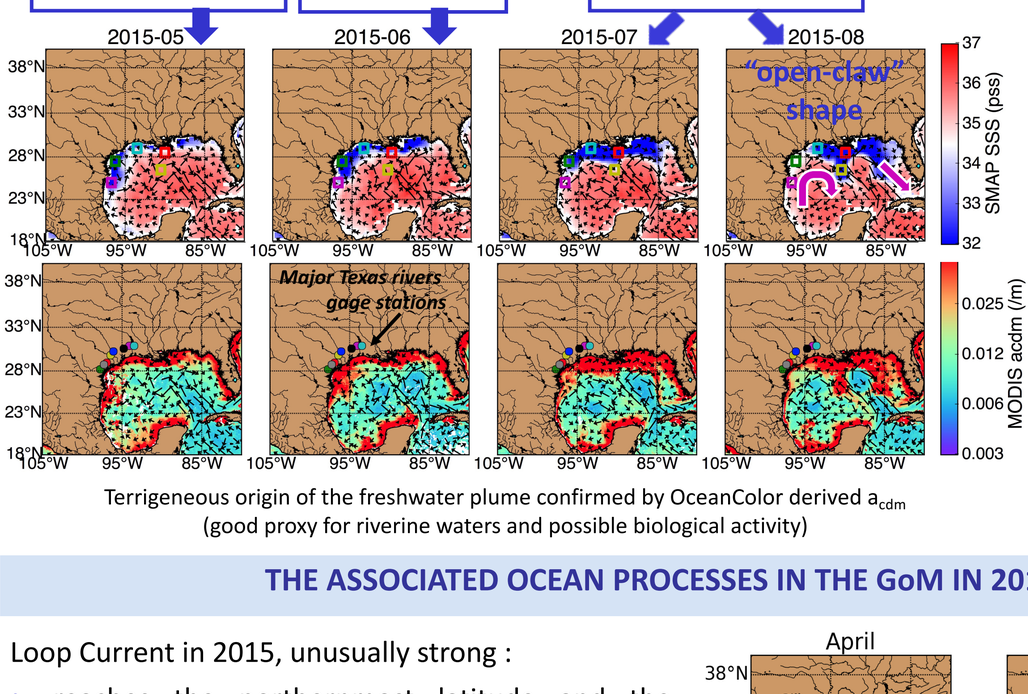

Terrigeneous origin of the freshwater plume confirmed by OceanColor derived a_{cdm} (good proxy for riverine waters and possible biological activity)

LAND / OCEAN

Square 1 – **May 2015**: SSS drops to 32 pss, 1 pss lower than in the preceding 4 years

Square 2 - **June 2015**: SSS drops to 28 pss, 3 pss lower than in the preceding 4 years

Square 3 - **July 2015**: SSS drops to 28 pss, 2 pss lower than in the preceding 4 years

Square 4 - **August 2015:** SSS drops to below 32 pss, 3-4 pss lower than those in the preceding 4 years: unusual freshwater transport

Square 5 – Near Mississippi mouth, 2015 SSS signal same as prior years, suggesting unusual freshwater tongue originates with Texas flood

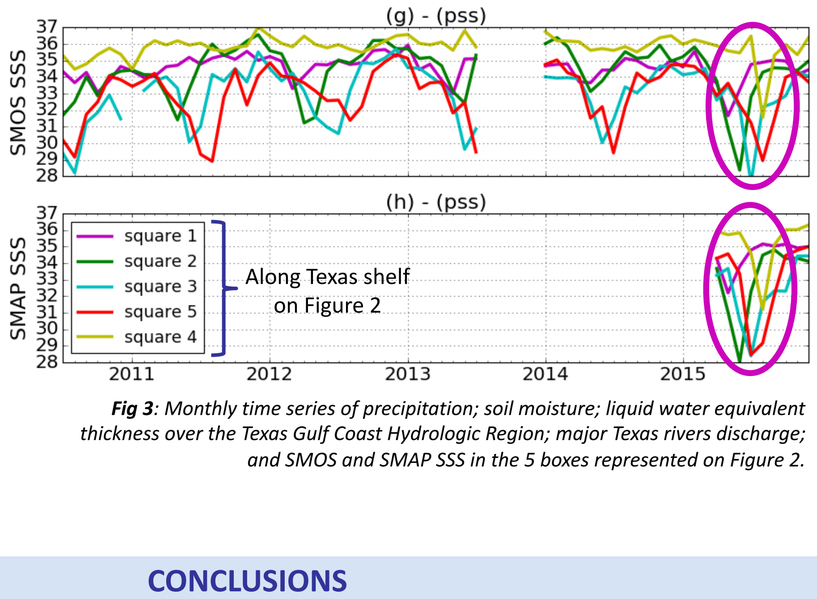

Fig 3: Monthly time series of precipitation; soil moisture; liquid water equivalent thickness over the Texas Gulf Coast Hydrologic Region; major Texas rivers discharge; and SMOS and SMAP SSS in the 5 boxes represented on Figure 2.

THE ASSOCIATED OCEAN PROCESSES IN THE GoM IN 2015

Loop Current in 2015, unusually strong :

- reaches the northernmost latitude and the westernmost longitude over 2010-2015
- speed exceeds 1.5 m/s and persists at the end of summer
- an unusually strong eddy sheds off in April, persists until the end of summer (0.5-0.6 m/s) and carries the intense freshwater plume from the Texas shelf after the large flooding event, southward in its eastern flank (↷)
- the eastern flank of the Loop Current carries the Mississippi River plume southeastward (↘)

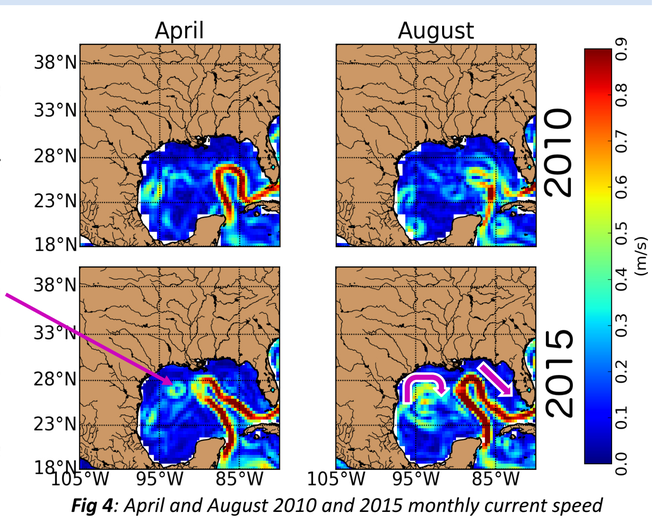

Fig 4: April and August 2010 and 2015 monthly current speed

→ the "open-claw", a rare occurrence shape of low SSS associated with the two strong freshwater water plumes

CONCLUSIONS

- This study utilizes atmospheric, terrestrial, & oceanic data from NASA satellites synergistically to characterize changes associated with the 2015 Texas flood event; the 1st study linking terrestrial & oceanic environments associated with flood.
- The large precipitation anomaly over Texas in May 2015 caused surface soil moisture to rise. The precipitation inputs did not infiltrate deeper soils and produced record runoff for the major hydrologic basins.
- An unusual freshwater plume offshore in the north-central GoM is observed, originated from the Texas shelf right after the flooding event, and carried northwestward along the coast then southward away from shore in August by the currents in the eastern flank of an anticyclonic eddy shed off from a particularly strong Loop Current earlier in the year.
- The unusual plume associated with the freshwater water originated from the Texas shelf can have potential implications on marine ecosystem (impacts of terrigenous matter carried by the freshwater plumes on marine ecosystem; northern GoM hypoxic zone).
- The space-based capability to monitor terrestrial hydrologic conditions may provide lead time for predicting the subsequent impacts on the northern GoM.

DATA

NASA SMAP SSS : 8-day, 0.25° resolution (JPL)
ESA SMOS SSS : 10-day, 0.25° resolution (LOCEAN, CECOS/CATDS)
In situ SSS in the GoM (NOAA NODC WOD09)
OSCAR currents : 5-day, 0.33° (PO.DAAC)
MODIS AQUA acdm at 443nm : 8-day running mean, 9km (Ocean Color)

NASA SMAP Soil Moisture : daily, 0.25° resolution (NSIDC)
ESA SMOS Soil Moisture : daily, 0.25° resolution (CATDS)
GRACE liquid water equivalent thickness : monthly, 1° (PO.DAAC)
Discharge levels of the Texas rivers : monthly (USGS)
TMPA 3B42 precipitation : daily, 0.25° resolution (GSFC DAAC)

National Aeronautics and Space Administration
Jet Propulsion Laboratory
California Institute of Technology
Pasadena, California

www.nasa.gov

Poster No. EA 16

National Aeronautics and Space Administration

Evaluation of SMAP sea surface salinity in river-dominated continental shelves

Yang Feng (329G), Dimitris Menemenlis (329C), Michelle M Gierach (329G)

Abstract

River-dominated continental shelves are highly productive regions due to influx of nutrients and organic matter from human activities. The physical condition of those shelves is highly variable as a result of riverine freshwater input, creating inconstant ecological environments. In this research, we investigate the river plume variability, an indicator of fate of riverine freshwater after entering the coastal ocean, from the high resolution sea surface salinity observation of the Soil Moisture Active Passive (SMAP) instrument for 5 large river-dominated continental shelves. Our study period starts on Apr 1st 2015, when SMAP data become available, and lasts for 1 year. A global configuration of the Massachusetts Institute of Technology general circulation model (MITgcm) with 18-km horizontal grid spacing forced by realistic point river sources, as well as World Ocean Data (WOD) base salinity profiles, have been used to assess SMAP's skill in capturing the surface salinity variation on- and off- shore. We find that SMAP can effectively resolve the river plume variability both spatially and temporally, showing that it is a potential tool for studying human-induced environmental issues in coastal oceans.

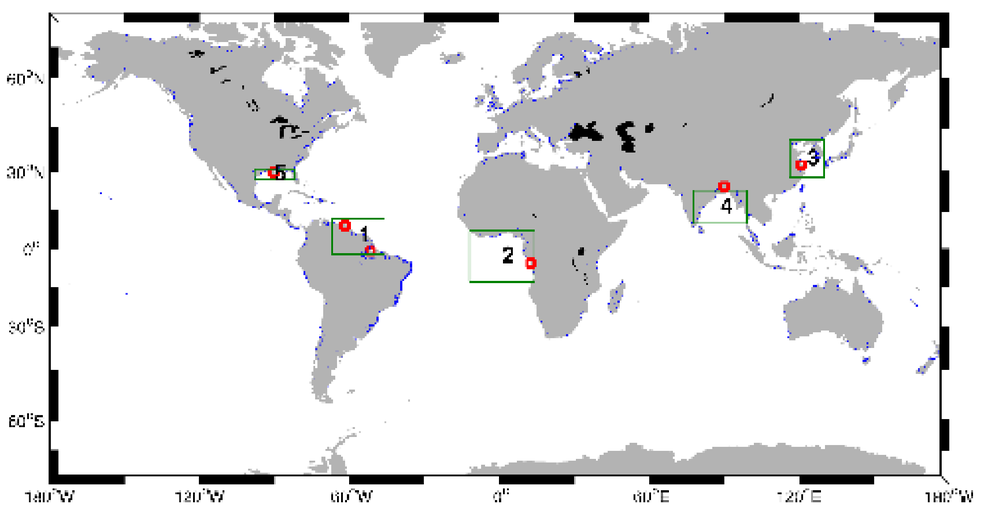

Figure 1: Global river distribution from Dai and Trenberth et al. [2009] and five selected river-dominated regions (green squares). Global rivers include world's largest 925 rivers (blue dots). Top 6 largest (red squares) sitting in five-selected regions were emphasized by red squares.

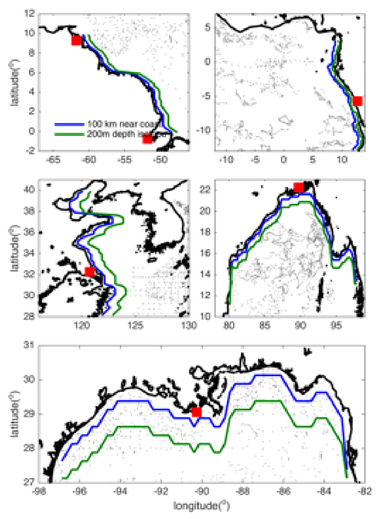

Figure 2: Enlarged five-selected river dominated regions in figure 1. Continental shelves are above 200 m isobath (black coastlines to green lines). We also separated regions 100 km away from coasts (black coastlines to green lines) for further studying river plume monthly variability from SMAP observation and ECCO simulation. Red squares were where top largest 6 rivers (Dai and Trenberth et al. [2002]). Randomly distributed black dots within each region were World Ocean Database samplings. Only the Mississippi River region has samplings above the continental shelf.

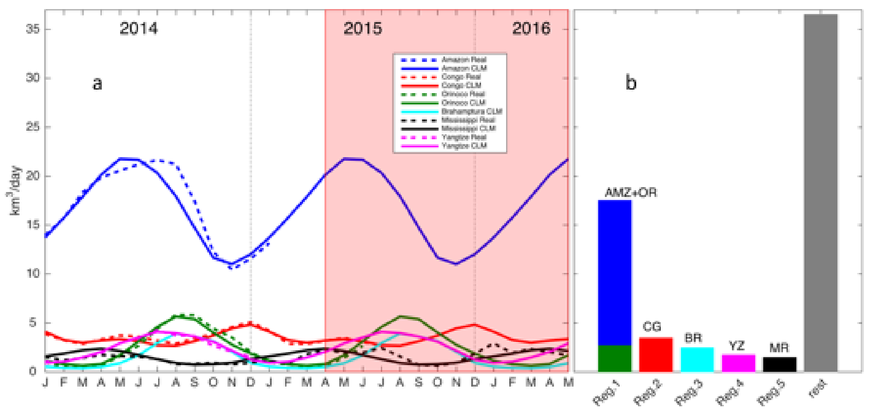

Figure 3: Climatological, real-time monthly (starting from January 2014) , and annual mean river flows of world largest rivers. (a) climatological (solid lines) river flows are according to Dai and Trenberth et al. [2009] (http://www.cgd.ucar.edu/cas/catalog/surface/dai-runoff/). Available real-time (dash lines) monthly river flow of Amazon, Congo and Orinoco are from http://www.ore-hybam.org; Yangtze is from http://www.cjh.com.cn/pages/nsgb.html; Mississippi is from USGS Baton Rouge, LA http://waterdata.usgs.gov/usa/nwis/uv?site_no=07374000; 1-yr SMAP data periods are highlighted by shaded red; (b) annual mean 925 world largest river flows from Dai and Trenberth et al. [2009]. Top 6 and the rest are separated by colors. Both Amazon and Orinoco Rivers went into region 1.

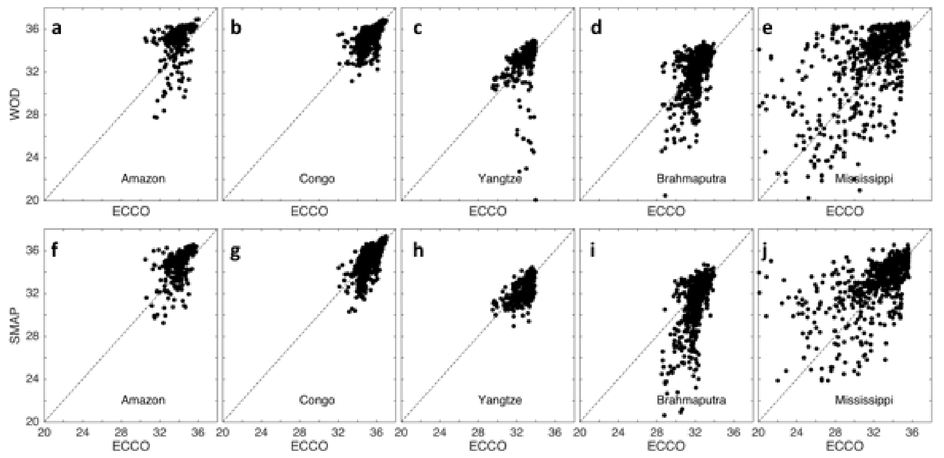

Figure 4: Point-by-point comparison for sea surface salinity between WOD and ECCO (a-e); as well as SMAP and ECCO (f-j). SMAP is 8-day averaged Level 3 data with 0.5° resolution; ECCO is daily model output on 18-km grids. They are both sampled at the same time and location closest to WOD. WOD sampling locations are shown on Figure 2.

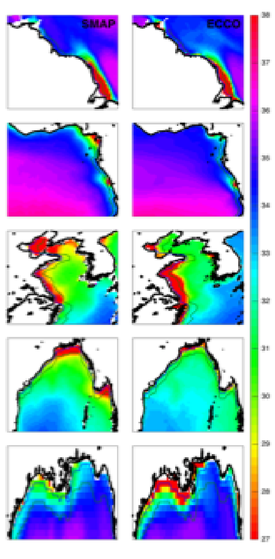

Figure 5: SMAP and ECCO Sea Surface Salinity annual mean.

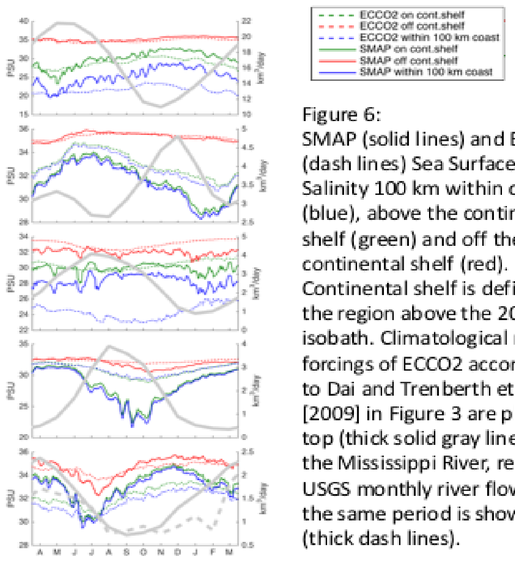

Figure 6: SMAP (solid lines) and ECCO (dash lines) Sea Surface Salinity 100 km within coast (blue), above the continental shelf (green) and off the continental shelf (red). Continental shelf is defined as the region above the 200 m isobath. Climatological river forcings of ECCO2 according to Dai and Trenberth et al. [2009] in Figure 3 are plot on top (thick solid gray lines). For the Mississippi River, realistic USGS monthly river flow in the same period is shown (thick dash lines).

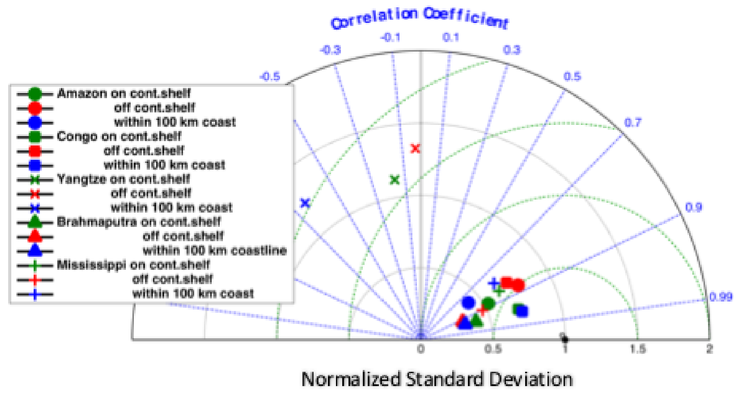

Figure 7: Taylor diagram for ECCO2-SMAP comparison at five selected regions. Original time-series is in figure 6.

National Aeronautics and Space Administration

Jet Propulsion Laboratory
California Institute of Technology
Pasadena, California

•**Poster No.** EA-17

www.nasa.gov

National Aeronautics and Space Administration

Monitoring of water surface slopes from AirSWOT:
First results over the Wax Lake Delta

Authors: Claire Michailovsky (334H)
Marc Simard (334F) Ernesto Rodriguez (3340)

Introduction / Motivation

Traditional in situ water level monitoring fails to reveal the full spatial complexity of water elevation and flow, especially in complex environments.

The AirSWOT instrument (see box) was designed to provide spatially distributed measurements of water surface elevation (WSE).

The Wax Lake Delta in Louisiana is one of the only areas along the Gulf Coast currently gaining rather than loosing land to the ocean.

→ Understanding its dynamics could help replicate land gains elsewhere.

Objective: demonstration of AirSWOT for measurement of inland water surface levels and slopes.

The AirSWOT instrument
Air Surface Water Ocean Topography

- Ka-band airborne radar interferometer
- 5 km wide swath (2 separate swaths)
- centimetric error
- cal/val for planned SWOT satellite
- gridded product: 3m pixels

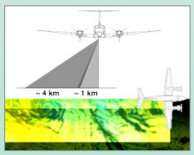

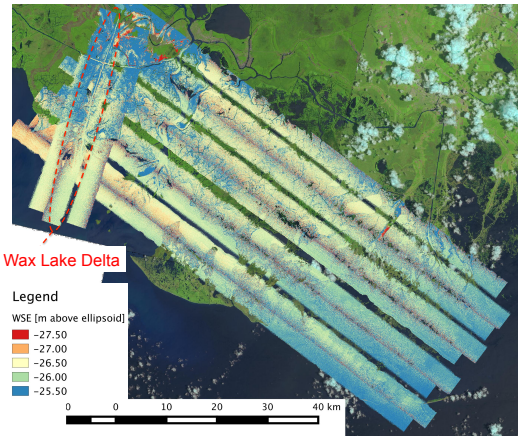

Fig 1: AirSWOT surface elevation data (2015/05/09) & location of the Wax Lake Delta

Data Collection / Extraction of surface slopes

AirSWOT flown in May 2015 following pattern shown in Fig. 1

Only wide swath data collected

UAVSAR flown over the same area

Water areas extracted based on UAVSAR derived mask

Water mask adjusted to avoid layover areas

Slopes extracted along main channel and delta branches

Results: Water Surface Slopes over the Wax Lake Delta

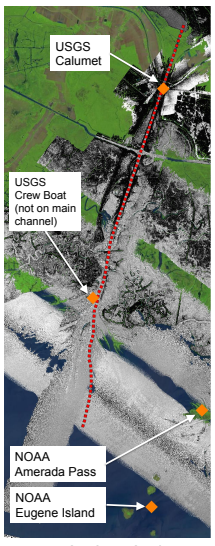

Fig 2: AirSWOT WSE & channel location

Crossover lines & USGS/NOAA stations

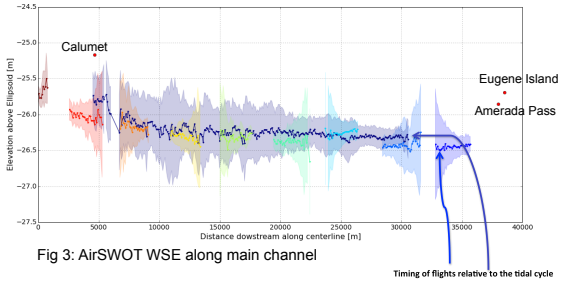

Fig 3: AirSWOT WSE along main channel

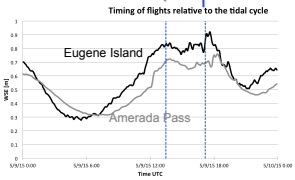

Water flows downstream… mostly!

Some discrepancies between crossover lines, explained partially by tidal cycle

~70 to 80cm bias relative to in situ stations

Averaging performed along and across channel, data spread large relative to slope in this case

Errors increase with high and low incidence angles (filtered out in Fig.3)

Conclusions

- AirSWOT is a promising new instrument for monitoring complex hydrodynamics
- Able to survey large areas: ~4 hours to fly all lines shown in Fig. 1
- Overall consistency between data from different flight lines
- Challenge in low slope areas
- Bias found relative to in situ datasets

Next steps / Planned applications

- Further analysis of discrepancies between crossover lines
- Assess performance over flooded grasslands
- Use of AirSWOT in conjunction with hydrodynamic models to estimate channel and lateral flows through flooded vegetation
- Use of AirSWOT with other instruments (AVIRIS) to estimate carbon transport from land to ocean (flights planned for October 2016)

Bonus: AirSWOT performance over land!

Comparison of LIDAR and AirSWOT data over areas identified as bare or low vegetation from UAVSAR shows good agreement.

80 cm bias identified between AirSWOT and LIDAR

→ Need to study Ka-band penetration through vegetation & potential capability for WSE measurement in wetlands/flooded grasslands

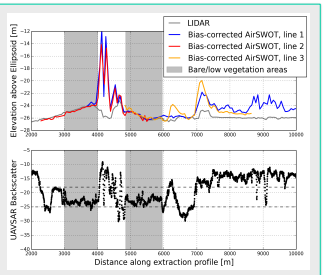

National Aeronautics and Space Administration
Jet Propulsion Laboratory
California Institute of Technology
Pasadena, California

www.nasa.gov

Poster No. EA-18

National Aeronautics and Space Administration

Detecting Earlier Drought from Water Demand Aspect

Author: Yixin 'Berry' Wen (329E)
Ali Behrangi (329E) and Bjorn Lambrigtsen (329E)

1. Back ground: Remote sensing of drought

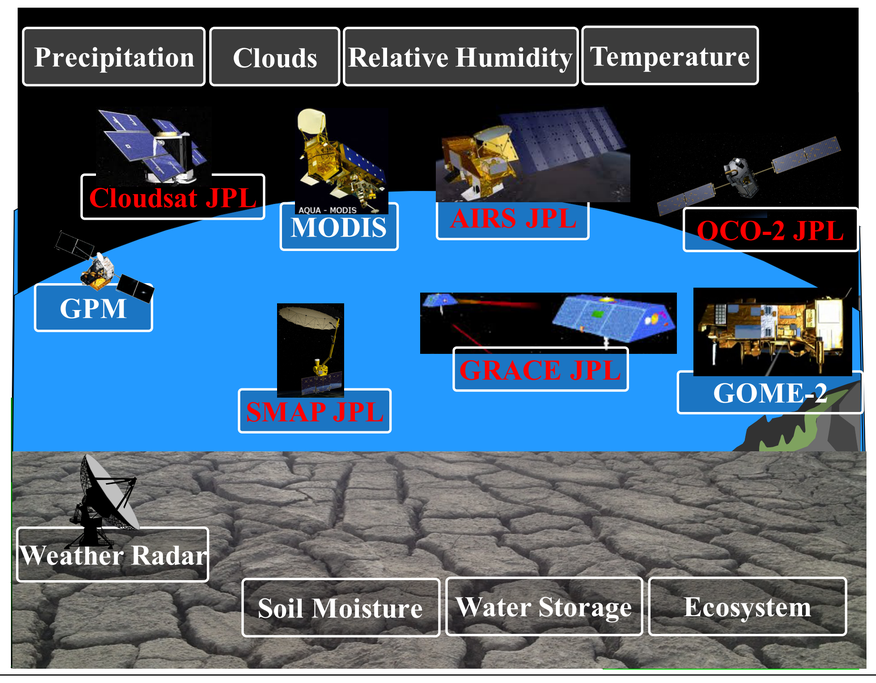

2. Objective

This study uses the drought of 2012 over the central Great Plains as a case study to explore the flowing scientific questions:

- Besides water supply aspect (e.g., precipitation), is there any other environmental variables to improve drought onset detection and early warning, for example, from atmospheric water demand aspect?
- Is the satellite-observed solar-induced chlorophyll fluorescence (SIF) able to monitor plant physiological stress from drought?
- How do natural ecosystem and artificial ecosystem respond to drought?

3. Benefits to NASA and JPL (or significance of results):

This study brings together multiple independent satellite data into a drought monitoring framework. Most of these satellite data are (or will be) from JPL missions (for example, Vapor Pressure Deficit (VPD) from AIRS, SIF from OCO-2, soil moisture from SMAP, and water storage changes from GRACE).

4. Results

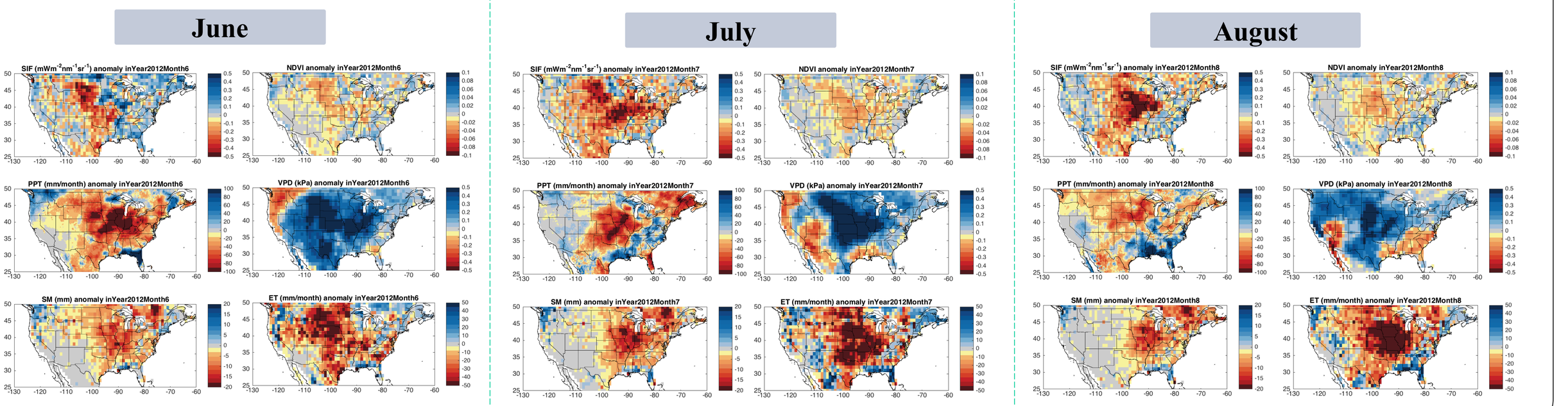

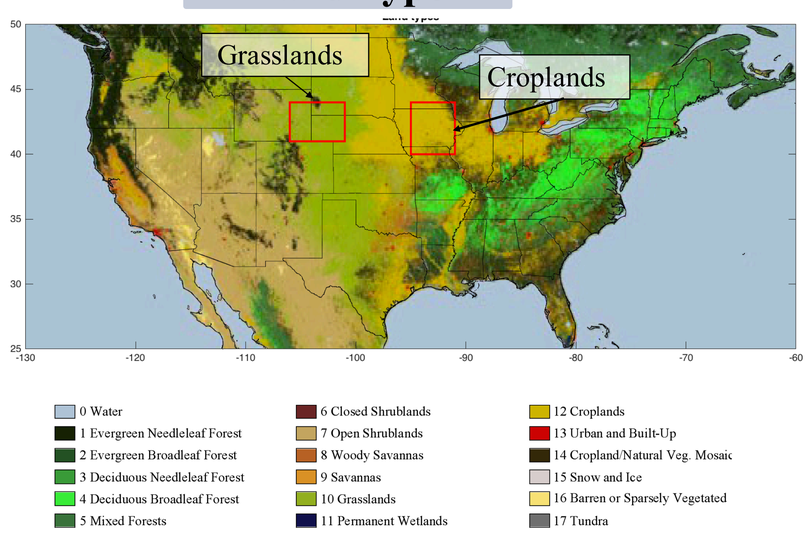

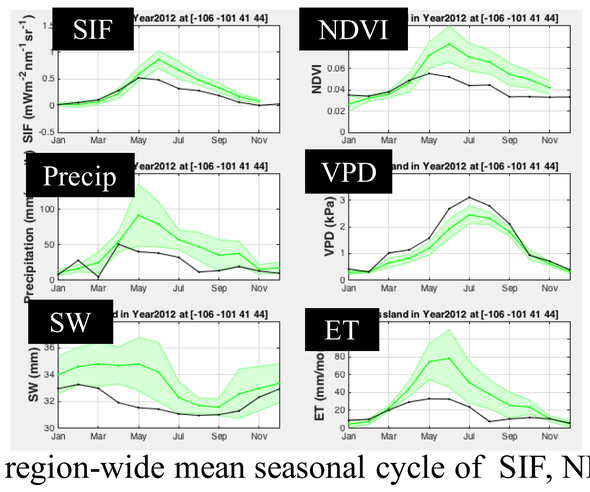

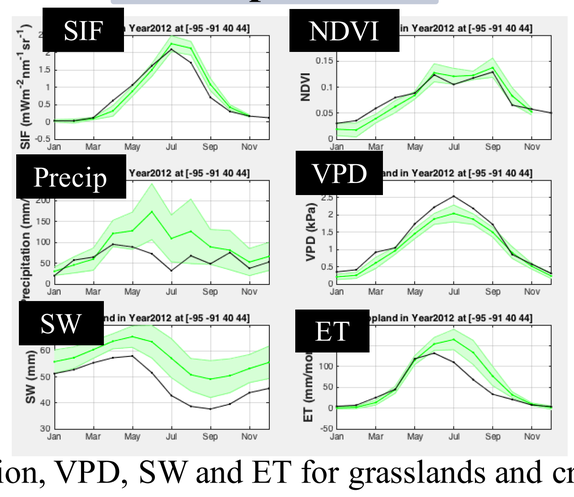

The region-wide mean seasonal cycle of SIF, NDVI, precipitation, VPD, SW and ET for grasslands and croplands. The green curves represent the monthly multiyear mean of each variable between 2007 and 2015; the black curves represent the seasonal evolution during 2012. The green shaded area is the +/1 std of the multiyear mean.

5. Conclusion and future work:

- This study indicates that the atmospheric water demand (VPD) detects the drought earlier than other environmental variables (e.g., precipitaiton and soil moisture). The drought pattern presented by VPD anomalies matches with the patter of SIF during peak drought months. It suggests that SIF characterizes the spatial and temporal dynamics of drought development. Compared to natural ecosystems (grasslands), the artificial ecosystem (croplands) show higher resistance to drought because of man-engineered irrigation.
- The future work will look at the finer scale data sets (e.g., weekly) to locate the tipping point where ecosystem photosynthesis shuts down during drought development.

National Aeronautics and Space Administration

Jet Propulsion Laboratory
California Institute of Technology
Pasadena, California

www.nasa.gov

The authors thank Ying Sun, Christian Frankenberg and Troy Magney for helpful discussion, Preeti Rao for providing VPD data, GOME-2 team for SIF data.

Poster No. EA-19

National Aeronautics and Space Administration

An Investigation of Global Inland Water Body Temperatures: Recent Trends and Future Projections

Nathan C. Healey (329G), Simon J. Hook (3200), John D. Lenters, Catherine O'Reilly Sebastiano Piccolroaz, Marco Toffolon

Objective

- Analyze the world's largest inland water bodies using thermal infrared satellite data and *in situ* measurements.

Study Sites

- Satellite data: approximately 169 worldwide, and 268 in North America.
- *In situ* data: approximately 118 water bodies.
- Summertime analysis: July-September (JAS) for North America, January-March (JFM) for Southern Hemisphere.

Materials and Methods

Inland Waterbody Surface Temperature Algorithm

$$T_s = a_o + a_1 T_{11} + a_2 (T_{11} - T_{12}) + a_3 (T_{11} - T_{12})(1 - sec(\theta))$$

$a_o, a_1, a_2,$ and a_3: split-window coefficients (lake and satellite specific).
T_{11} and T_{12}: 11 and 12 μm brightness temperatures.
θ - sensor view angle [*Hulley et al.*, *2011*].

Figure 1. *Photos of the Lake Tahoe and Salton Sea Calibration/Validation Instrumentation.*

Table 1. *Processing criteria for satellite temperature analysis (example: MODIS).*

Location	3 x 3 pixel window
Minimum points in JAS Range	20
Smoothing	LOWESS interpolation
Image Time	Night
Range from Target Coordinates	< 1 km
Standard Deviation in 3 x 3	< 0.5 K
Sensor Zenith Angle	< 45°
Cloud Masking	Cirrus Cloud Test High Cloud Test Thermal Test
Temperature Range	<= 308.15 and >= 237.15 K

Modelling Water Temperature in the Future

air2water [*Piccolroaz et al.*, *2013*] estimates Lake Surface Temperature (LST) using only air temperature.

$$\rho c_p V_s \frac{dT_w}{dt} = A \mathrm{H}_{net}$$

$$\frac{dT_w}{dt} = \frac{1}{\delta}\left\{a_1 + a_2 T_a - a_3 T_w + a_5 \cos\left[2\pi\left(\frac{t}{t_y} - a_6\right)\right]\right\}$$

$\boldsymbol{\rho}$ *:water density*
$\boldsymbol{c_p}$ *:specific heat capacity*
$\boldsymbol{V_s}$ *:surface volume*
$\boldsymbol{T_w}$ *:LST*
$\boldsymbol{t}$ *:time (t_y is yearly duration in days)*
$\boldsymbol{A}$ *:surface area of the lake*
$\boldsymbol{H_{net}}$ *:upper water volume net heat flux*
$\boldsymbol{a1 - a6}$ *:calibration parameters*

National Aeronautics and Space Administration
Jet Propulsion Laboratory
California Institute of Technology
Pasadena, California

www.nasa.gov

Results

Summertime Trends: 1985-2009

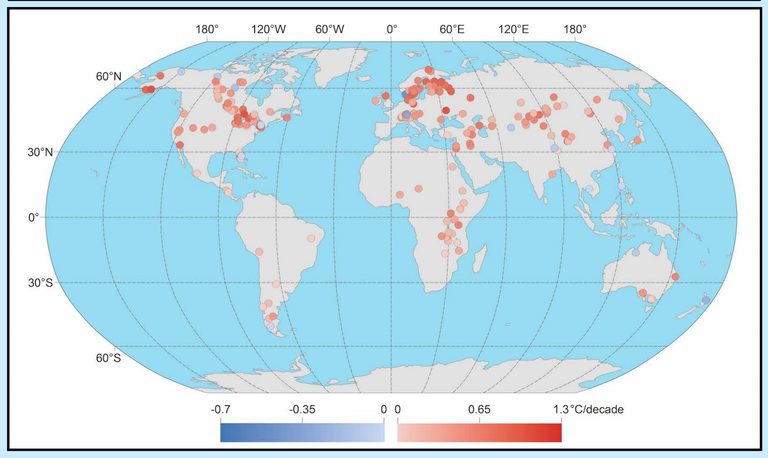

Figure 2. *Summertime surface temperature trends (1985-2009) for inland water bodies across the world [O'Reilly et al., 2015].*

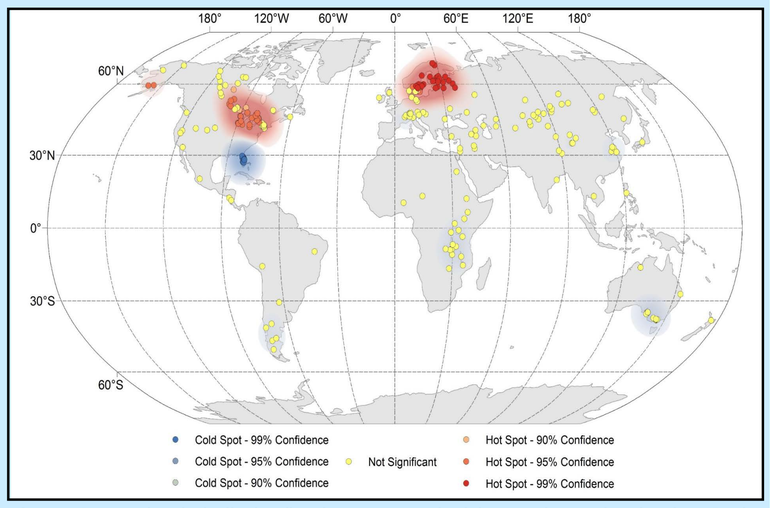

Figure 3. *Proximal similarity (i.e.'hotspot' analysis) was determined using Getis-Ord Gi* z-scores for all lakes. [O'Reilly et al., 2015].*

Relationship between Winter Air and Summer Water Temperatures: 2000-2015

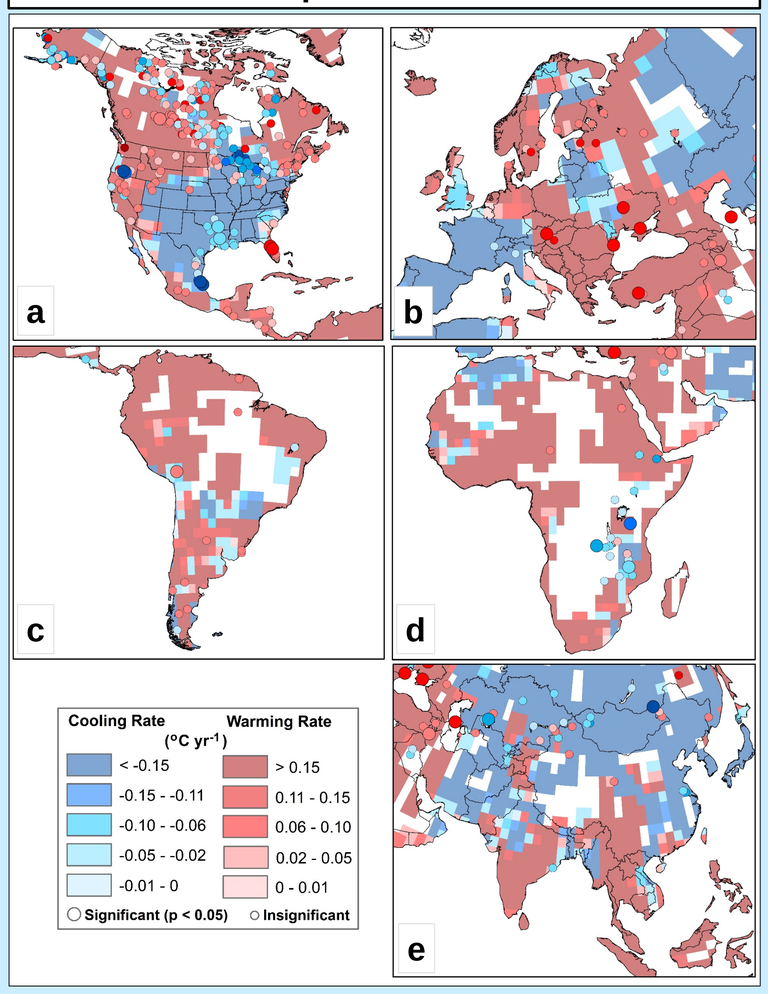

Figure 4. *Trends in 1993-2015 winter (NH: December-February, SH: June-August) air temperature [GISTEMP Team, 2015] and satellite-derived (ATSR, MODIS, VIIRS) summer (NH: July-September, SH: January-March) inland water body surface temperature for the five largest water bodies in (a) North America, (b) Europe, (c) South America, (d) Africa, and (e) Asia.*

- Regional climate forcing supplies the basic structure to the LST but local differences between lakes are important enough in winter to result in lake-specific modifications to the basic thermal structure.

Model Predictions with Climate Change

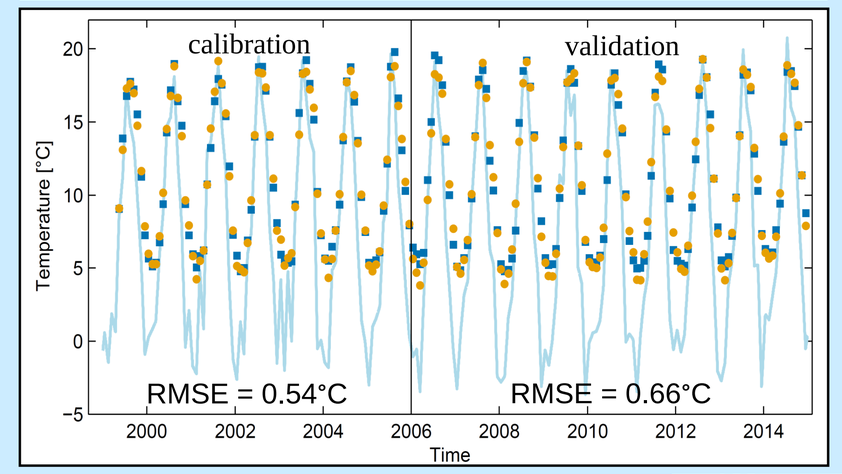

Figure 5. *Comparison between air temperature and observed and simulated water temperature for the case of UC Davis (air temperature) and NASA buoy (water temperature)*

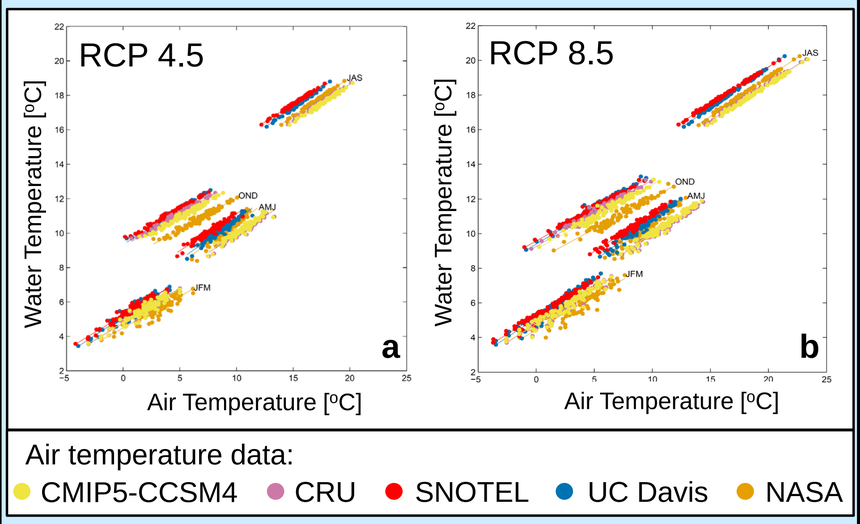

Figure 6. *Seasonal* relationships between air temperature and modeled lake surface temperature for two climate change scenarios: (a) RCP 4.5 and (b) RCP 8.5.

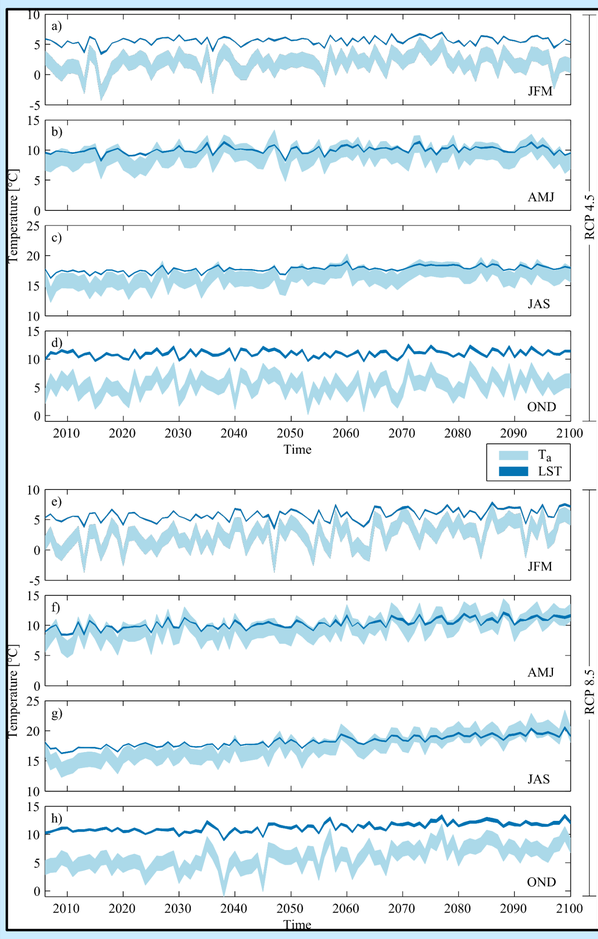

Figure 7. *Time series results of* modeled lake surface temperature for the climate change scenario RCP 4.5

Summertime warming: ~1 °C century^{-1}

Figure 8. *Time series results of* modeled lake surface temperature for the climate change scenario RCP 8.5

Summertime warming: ~3 °C century^{-1}

Conclusions

- From 1985-2009, almost all inland water bodies show summertime warming, but recent trends have flattened or even indicated cooling.
- Winter air temperatures seem to influence summer time inland water body surface temperatures.
  - o High heat capacity of water – lag in response.
- *air2water* is a robust tool to predict inland water body surface temperature when only air temperature is available.

Poster No. EA-20